Quantifying Chalcophile Elements and Heavy Halogens by Secondary Ion Mass

Spectrometry and Demonstrating the Significant Effect of Different Secondary Ion

Normalizing Procedures

by

Eric N. Carlson

A Thesis Presented in Partial Fulfillment
of the Requirements for the Degree
Master of Science

Approved July 2021 by the
Graduate Supervisory Committee:

Richard Hervig, Chair
Donald Burt
Kurt Roggensack

ARIZONA STATE UNIVERSITY

August 2021

ABSTRACT

A novel technique for measuring heavy trace elements in geologic materials with secondary ion mass spectrometry (SIMS) is presented. This technique combines moderate levels of mass resolving power (MRP) with energy filtering in order to remove molecular ion interferences while maintaining enough sensitivity to measure trace elements. The technique was evaluated by measuring a set of heavy chalcophilic elements in two sets of doped glasses similar in composition to rhyolites and basalts, respectively. The normalized count rates of Cu, As, Se, Br, and Te were plotted against concentrations to test that the signal increased linearly with concentration. The signal from any residual molecular ion interferences (e.g. $^{29}\text{Si}^{30}\text{Si}^{16}\text{O}$ on ^{75}As) represented apparent concentrations $\leq 1\,\mu\text{g/g}$ for most of the chalcophiles in rhyolitic matrices and between 1 and $10\,\mu\text{g/g}$ in basaltic compositions. This technique was then applied to two suites of melt inclusions from the Bandelier Tuff: Ti-rich, primitive and Ti-poor, evolved rhyolitic compositions. The results showed that Ti-rich inclusions contained $\sim 30\,\mu\text{g/g}$ Cu and $\sim 3\,\mu\text{g/g}$ As while the Ti-poor inclusions contained near background Cu and $\sim 6\,\mu\text{g/g}$ As. Additionally, two of the Ti-rich inclusions contained $>5\,\mu\text{g/g}$ of Sb and Te, well above background. Other elements were at or near background. This suggests certain chalcophilic elements may be helpful in unraveling processes relating to diversity of magma sources in large eruptions. Additionally, an unrelated experiment is presented demonstrating changes in the matrix effect on SIMS counts when normalizing against $^{30}\text{Si}^+$ versus $^{28}\text{Si}^{2+}$. If one uses doubly charged silicon as a reference, (common when using large-geometry SIMS instruments to study the light elements Li - C) it is important that the standards closely match the major element chemistry of the unknown.

ACKNOWLEDGEMENTS

TABLE OF CONTENTS

LIST OF TABLES

LIST OF FIGURES

Chapter 1

INTRODUCTION

The heavy chalcophile and halogen elements including Cu, As, Se, Br, Sb, and Te are some of the least abundant elements in the solar system and the earth's crust (Anders and Grevesse, 1989; Wedepohl, 1995). While the number of analyses of natural materials from Earth and other planetary bodies is increasing, there are still questions about the absolute amounts of these elements in different terrestrial reservoirs (Rudnick and Gao, 2003).

In this chapter, the potential for using a combination of two different techniques for removing molecular ions from the mass spectrum is tested on a variety of silicate glass standards. The results suggest that low detection levels (µg/g and below) for heavy chalcophile elements are indeed possible using this approach in some cases, but in others the results are only nearly as good as traditional approaches. One application of this analytical technique to the large Bandelier eruption in northern New Mexico is presented and additional areas for application are suggested in chapter 2.

1.1   Chalcophile Elements

The chalcophile elements as a group are classified by their preference for sulfur based minerals and melts in contrast to the lithophiles (those preferring silicates) and the siderophiles (those preferring iron) (Barnes, 2017). Which elements behave as chalcophiles depends on the P/T conditions and oxygen fugacity of the melt, and in particular many elements that are highly siderophile at core and solar system conditions behave as chalcophiles at the higher $f\mathrm{O_2}$ of the crust and mantle where

iron-alloys are not stable (Barnes, 2017). These elements can be classified by their partition coefficients between sulfide and silicate melts, with elements in the 1–10 range being classified as weakly chalcophile, those in the 20–100 range being moderately chalcophile, those in the 100–1000 range as strongly chalcophile, and those in the >1000 range as highly chalcophile. Partition coefficients for the chalcophiles

Partition Coefficients of the Chalcophiles
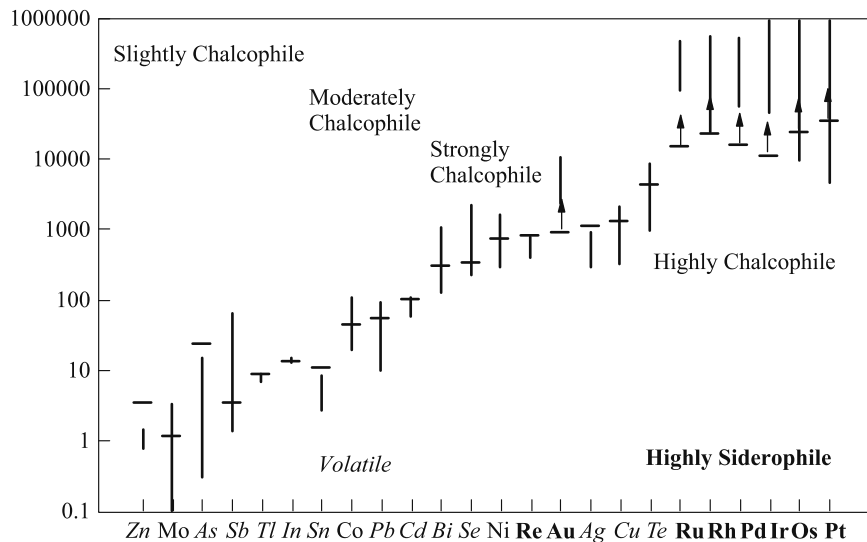
Figure 1.1: Figure taken from Barnes (2017) based on data compiled by Barnes and Ripley (2016) showing the partition coefficients between sulfide and silicate melts (vertical axis) for the chalcophile elements. Horizontal dashes represent the coefficient determined from MORB. Vertical lines represent the range of coefficients determined by experiments conducted with $\log f\mathrm{O}_2$ ranging from the fayalite-magnetite-quartz buffer ± 2. Vertical arrows indicate minimum coefficients. Additionally, elements in bold are highly siderophile, and those in italics are volatile.

determined by experiment and empirically from MORB are shown in figure 1.1.

From the chalcophiles, we have selected S, Cu, As, Se, Sb, and Te to study. While any number of heavy elements would work in testing our SIMS technique, we specifically chose these chalcophiles with an eye towards later applying the technique to a suite of melt inclusions from the Lower Bandelier Tuff. These elements all form intense negative ions (important for SIMS as we can only measure one polarity of

ions at a time) and range from slightly to strongly chalcophilic. Additionally, all are classified as volatile, which is defined by having low condensation temperatures from the solar nebula (Lodders, 2003). This volatility leads them to preferentially partition into any vapor phase that might be present in a magmatic system (Barnes, 2017). Additionally, while there is little data available on the partitioning of these elements between a silicate melt and magmatic-hydrothermal fluids, at least some of the chalcophiles (including S, Cu, Mo, Zn, Ag, and Au) have been found to preferentially partition into these fluids in Cu-Mo porphyries (Barnes, 2017). As will be discussed in more detail later, Dunbar and Hervig (1992) found that melt inclusions from the Lower Bandelier represent two distinct melts with different lithophile trace elements signatures interpreted to represent an evolved magma and a later injection of primitive magma. Since Dunbar and Hervig (1992) looked at only the lithophiles and highly volatile elements (Cl, H, F), we believe these vapor/fluid preferring elements might tell us more about the sources of these two magmas.

Chapter 2

COMBINING ENERGY FILTERING WITH HIGH MASS RESOLVING POWER

The primary analytical technique used in this thesis is secondary ion mass spectrometry (SIMS). This will be described in detail in the following sections. Analyses on the electron microprobe were also performed. This is a routine technique that will be covered in significantly less detail in chapter 3.

2.1 Secondary Ion Mass Spectrometry (SIMS)

SIMS is a microanalytical technique that has been applied commonly in materials science, geochemistry, and cosmochemistry (Williams, 1985; Shimizu and Hart, 1982). The reason for its popularity is because of its flexibility (ions that form intense positive or negative ions can be studied, thus covering much of the periodic table) and its ability to work with volumes of sample on the lateral and depth scale of small phases within a polished thin section (i.e., samples a few tens of microns across and less than 30 microns thick).

2.1.1 Background on SIMS Analyses

A common application of SIMS is the study of volatile elements in volcanic rocks, including study of matrix glass (for degassing and re-hydration phenomena), glass inclusions in phenocrysts (as representatives of liquid compositions prior to eruption-related degassing), and even hydrous and nominally anhydrous phenocrysts (to estimate the H_2O content of primitive magmas and to unravel degassing events). SIMS analyses of volatiles have included measurements of hydrogen, carbon, fluorine, sul-

fur, and chlorine as well as the isotopes of these elements (Koga *et al.*, 2003; Riciputi *et al.*, 1998; Hoskin, 1999; Hauri *et al.*, 2002; Kumamoto *et al.*, 2017). The above applications of SIMS have typically studied negative secondary ions. This is because halogens and chalcophile elements have high ionization potentials (precluding positive ion analysis) but high electron affinities. One reason that H, C, F, S, and Cl have been emphasized is that the impediments to quantitative analysis are relatively easily overcome. The sputtering process that creates ions in SIMS is inherently chaotic, and produces a large number of molecular ions as well as elemental ions and electrons. Some of these molecular ions can have the same nominal mass to charge ratio as the ion of the isotope that is being measured, resulting in an interference. The mass to charge ratio of these molecular ions is never exactly the same though, and the peaks of elemental ions can be separated from them with sufficient mass resolving power (MRP). For the light elements, there are fewer elements lighter than themselves and thus less combinations that could produce a singly charged molecular ion of the same mass. For example hydrogen can be studied as the elemental H^- ion for which there are no molecular ions of the same mass/charge ratio (e.g. Hauri *et al.* (2002)). Hydrogen is also studied as the hydroxide ion (typically $^{16}OH^-$, e.g. Tenner *et al.* (2009)). However in this case there is a serious interference at mass/charge = 17 from the minor oxygen isotope $^{17}O^-$. Table 2.1 lists molecular interferences for some of these light elements (C, F, S, Cl) in comparison to the interferences of a selection of heavier chalcophiles that must be removed prior to obtaining quality analyses, as well as the MRP required to separate the closest of these interferences from the element. Table 2.1 illustrates that with increasing mass, the number of potential interfering molecular ions increases and the MRP required also increases. Determining the concentrations of the much heavier chalcophiles becomes quite challenging because of the suspected interferences. In many cases, mass resolving powers in excess of 10,000, going as

5

high as 190,000 in the case of ^{130}Te, are required to separate the chalcophiles from all potential molecular ions. However, it should be noted that many potential mass interferences come from rare isotopes and elements that are present in only trace amounts in geologic materials. Thus these interferences may not be important and the necessary MRP could be significantly lower in many cases.

Another way of resolving the signal of an element from molecular ions is to directly remove the molecular ions through energy filtering. In SIMS the process of sputtering ions off the surface produces ions with a wide range of energies. Because

Comparison of Mass Interferences of the Light Elements and Chalcophiles

	Species	Potential Interferences	Minimum MRP
Light Elements	^{12}C$^-$	^{11}BH$^-$	701
	^{19}F$^-$	^{7}Li^{12}C$^-$	1080
	^{32}S$^-$	^{31}PH$^-$, ^{16}O$_2^-$, ^{13}C^{19}F$^-$	3362
	^{35}Cl$^-$	^{32}SH$_2^-$, ^{23}Na^{12}C$^-$, ^{16}O^{19}F$^-$, ^{11}B^{12}C$_2^-$	5120
Chalcophiles	^{65}Cu$^-$	^{64}NiH$^-$, ^{64}ZnH$^-$, ^{53}Cr^{12}C$^-$, ^{49}Ti^{16}O$^-$, ^{32}S^{33}S$^-$, ^{41}K^{12}C$_2^-$, ^{49}Mg$_2$^{16}O$^-$, ^{29}Si^{12}C$_3^-$	8125
	^{75}As$^-$	^{48}Ti^{27}Al$^-$, ^{29}Si^{30}Si^{16}O$^-$	9630
	^{80}Se$^-$	^{40}Ca$_2^-$, ^{56}Fe^{24}Mg$^-$	9186
	^{121}Sb$^-$	^{57}Fe^{16}O$_4^-$, ^{28}Si^{29}Si^{16}O$_4^-$	10670
	^{130}Te$^-$	^{94}Zr^{12}C$_3^-$, ^{28}Si^{27}Al$_2^{16}$O$_3^-$	188406

Table 2.1: Table of the mass interferences and minimum required MRP comparing some of the commonly measured light elements with the selection of chalcophilic elements studied in the following chapters. As mass increases, so do the number of possible molecular ions and the difference in mass between the elemental ion and molecular ion becomes smaller. For the chalcophiles, only Cu lists most of the potential interferences to illustrate this point. The rest of the chalcophiles only have the closest interferences relevant to geologic matricies listed

of this, conventional SIMS instruments feature an electrostatic analyzer (ESA) before the magnetic sector. Like the magnetic sector this bends the path of the ions, but the amount it bends depends on the energy of the ion rather than its mass. A slit between the ESA and magnet selects ions in a certain range of energies, allowing only those to be measured. Molecular ions have been found to form with a narrower energy distribution than elemental ions, and this range gets narrower the more complex the molecule is (Crozaz and Zinner, 1985). Thus it is possible to filter out many potential interferences by only measuring a small range of high energy ions. This can be very effective for measuring heavy elements in some materials where the most important interferences are complex and heavy. For example it has been demonstrated that this allows the precise measurements of rare earth elements in oxides and phosphates at concentrations on the order of $0.1\,\mu g/g$ (Crozaz and Zinner, 1985; Zinner and Crozaz, 1986). However, energy filtering is ineffective for removing small molecules and molecules where the difference in mass between the atoms is very large, in particular hydrides (Crozaz and Zinner, 1985).

2.1.2 Combining High Mass Resolving Power with Energy Filtering

Because of the high MRP required to resolve molecular interferences from heavy elements, analyzing trace amounts of these elements is seemingly impossible for a normal SIMS. In order to increase MRP, the entrance and exit slits in the secondary column must be narrowed, blocking out ions and reducing sensitivity. At the required MRP, the sensitivity is far too low to detect trace amounts of chalcophiles or other heavy elements. One solution has been to use specialized "large geometry" SIMS (LG-SIMS) that have much larger magnets, keeping the ions in the magnetic field for longer allowing for greater dispersion of the ions before they reach the detector. Thus

these instruments can reach much higher levels of MRP without sacrificing counts. However, they are relatively uncommon and quite expensive. Energy filtering can be an effective alternative to high MRP in some cases, but is limited by the fact it works best to remove molecules containing 3 or more atoms (Crozaz and Zinner, 1985). If there are additional simple molecules like dimers and hydrides that are also interfering with the ion of interest, then energy filtering alone may not work.

Due to the deficiencies of each method on their own, we propose combining energy filtering with moderately high MRP to enable measuring trace levels of heavy elements like the chalcophiles on the more common small geometry SIMS. Energy filtering will remove the majority of the complex molecular ions. Any remaining small molecular ions may only need a moderately high level of MRP to separate them, such as is reasonably attainable on a small geometry SIMS. This has never seriously been considered before, likely due to the fact that both high MRP and energy filtering reduce detection efficiency. However, there may be enough ion counts left over to make accurate measurements of trace elements in geologic materials. We will first test this technique by measuring a number of heavy chalophilic elements, including Cu, As, Se, Sb, and Te, in two suites of standard glasses analogous to rhyolites and basalts. From these analyses, we will be able to determine the molecular ion background remaining and the level of accuracy attainable using this method. We will then show an example applying this technique to measuring the chalcophiles in a set of melt inclusions from the Lower Bandelier Tuff.

2.2 Methods

2.2.1 General SIMS Analysis Procedure

Each of our analyses followed roughly the same procedure. First, an aluminum-copper calibration grid was loaded into the instrument to use as an alignment target while we focused and aligned the primary and secondary beams. We then maximized the current of Cs^+ ions exiting the primary column. This was done by tweaking the voltage of the first three lenses in the column, first adjusting the three lenses in order from closest to farthest from the sample and then iteratively adjusting each lens and associated deflector plates until a maximum current had been reached. This maximum was usually somewhere in the range of 100-300 nA, depending on the selected aperture sizes in the primary column. The voltage on lens 3 was then increased, simultaneously reducing the primary beam current and the diameter of the beam, until the beam current was about 5 nA. Next, we began measuring the current of the secondary beam with an easily produced ion from the grid like $^{16}O^-$ or $^{27}Al_2^-$ using the faraday cup. The strength of the spectrometer's magnet was then adjusted to find the peak current, and this magnetic field was then calibrated against the exact mass. Next, the location of the primary beam hitting the sample was centered with the deflectors associated with lens 4. This was done using the microchannel plate to produce a chemical image of the ions coming from the beam's location. Once the beam had been centered, it was then further shaped by adjusting the stigmators and voltage on lens 4 to produce a beam that was as small and round as possible, and uniformly expands about its center when the voltage on lens 4 is changed. The beam was then rastered over a wide area to produce an image of the grid, and the stigmators in the secondary column were adjusted to make the copper grid bars appear as sharp, orthogonal, and square as possible.

Once the beam had been properly centered and shaped, the next step was to set the energy filtering and mass resolving power of the instrument. A 400 μm field aperture was first inserted. The spectrometer's energy window was then fully closed then opened slowly until counts just appeared on the electron multiplier. The window was then translated until the counts were maximized, thus centering the energy window. Next, the window was translated and opened by a certain number of turns determined by earlier experimentation to produce the optimal amount of energy filtering. This was determined to be a $-27\,$V offset with a 40 eV bandpass by taking energy spectra of $^{27}Al_3^-$ with and without the energy window offset (see Figure 2.1). The entrance and exit slits were then adjusted to produce a mass resolving power of about 3000. This was reached by iteratively changing the width of the slits and measuring the mass resolving power, determined by taking a high resolution mass spectrum of an easily measured ion like ^{18}O and measuring the width of the peak at 10% of the maximum (see Figure 2.2).

In addition to the shaping and aligning the primary beam, we also needed to shape and align the electron gun beam. As our samples and standards are insulators, we needed to use the instrument's electron gun to compensate for positive charge building up on the sample surface. The positive primary beam brings an excess of positive charge to the sputter crater, and unlike negative primary beams where the excess charge is carried away by secondary electrons there is no easy way for this charge to escape. The electron gun is set up such that the electrons are accelerated toward the sample with not quite enough velocity to overcome the -5kV potential being applied to the sample. If even a small positive charge builds up from the primary beam, the electrons will be able to reach the surface and neutralize the charge. As a side note, it is because of this fine balance between the voltage on the sample and the accelerating voltage of the electron beam we are forced to do energy filtering by purposely mis-

aligning the energy window. Energy filtering can also be achieved by simply reducing the accelerating voltage on the sample, such as described in Zinner and Crozaz (1986) and Shimizu and Hart (1982). If we did this, the high current electron beam would impact the sample with considerable energy, heating and possibly damaging it. As translating the energy window mis-tunes the spectrometer to a degree, we applied considerably less energy filtering than in the previously referenced paper.

In order to shape the electron beam and center it on the primary beam impact crater, we followed the procedure of Chen *et al.* (2013). The calibration grid was removed and a sample mount containing grains of a number of standard glasses and benitoite, a highly cathodoluminescent mineral, was inserted. The instrument was then focused on the benitoite grain. The electron gun was turned on with the primary ions turned off. The sample voltage was then increased from -5kV to -1kV, allowing the electrons to reach the sample without the primary beam charging the surface. The sample was viewed through an optical microscope without illumination. The electron beam striking the benitoite produces a visible cathodoluminescent glow. This acts as an image of the electron beam on the sample, allowing us to visually align the electron beam with the impact location of the primary beam. It also shows how uniform the beam is, which we manimpulated by tweaking the magnetic and electrostatic lenses guiding the beam.

Once this setup was complete, we then began taking measurements of standards and unknowns. First, the target was located on the sample and the sample was moved so the beam location was on the surrounding matrix in order to locate its exact position. With the largest (1800 µm) field aperture in place, the ions were turned on and the beam position was centered using the lens 4 deflectors while looking at an abundant and easily formed ion like $^{16}O^-$. The position of the resulting crater was then noted in the optical microscope. The ions were turned off and the sample

(a) Energy Window Bandpass
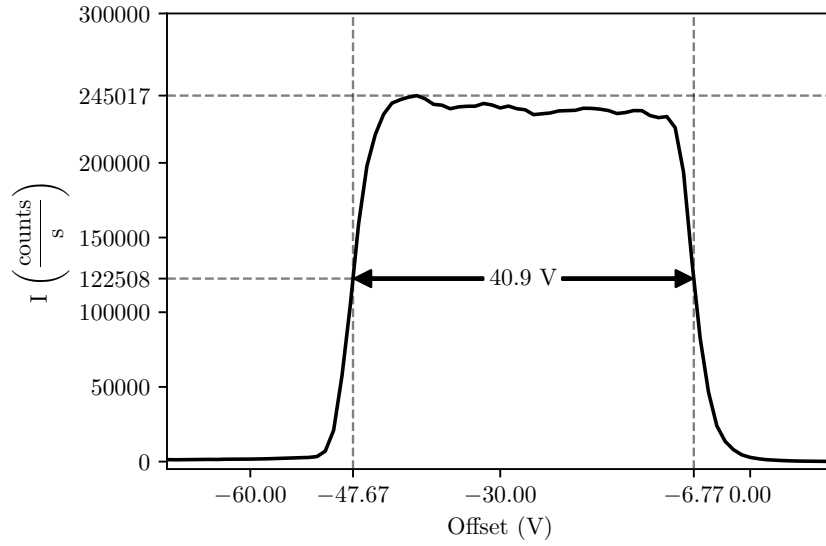
(b) Energy Window Offset
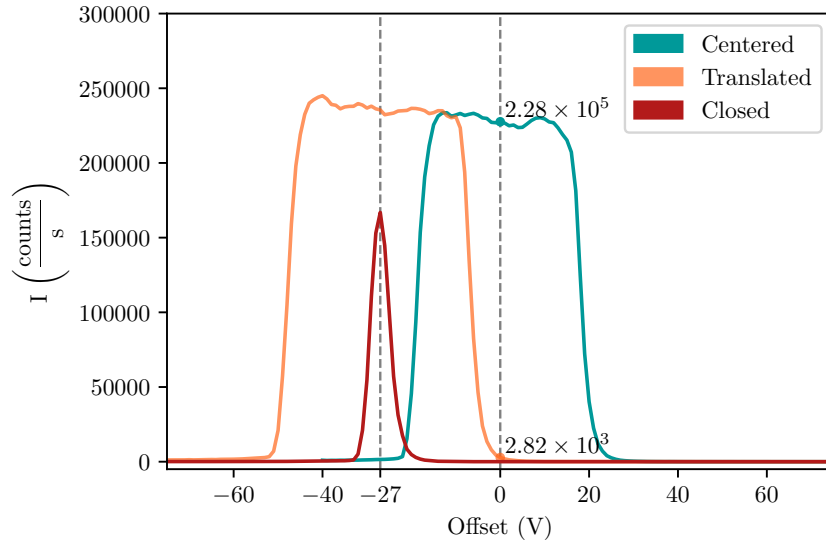
Figure 2.1: Energy spectra of the molecular ion $^{27}\text{Al}_3^-$ taken under different conditions. (a) Illustration of the process of determining the energy bandpass. The voltage offset corresponding to half the maximum counts is found on either side of the peak, and the bandpass is their difference. (b) Energy spectra with the window centered (cyan), translated by 1 turn (orange), and translated and closed (red). Comparing the centered and translated window with a $-27\,\text{V}$ bandpass at a 0V offset, $^{27}\text{Al}_3^-$ ion intensity is decreased by a factor of ~100

12
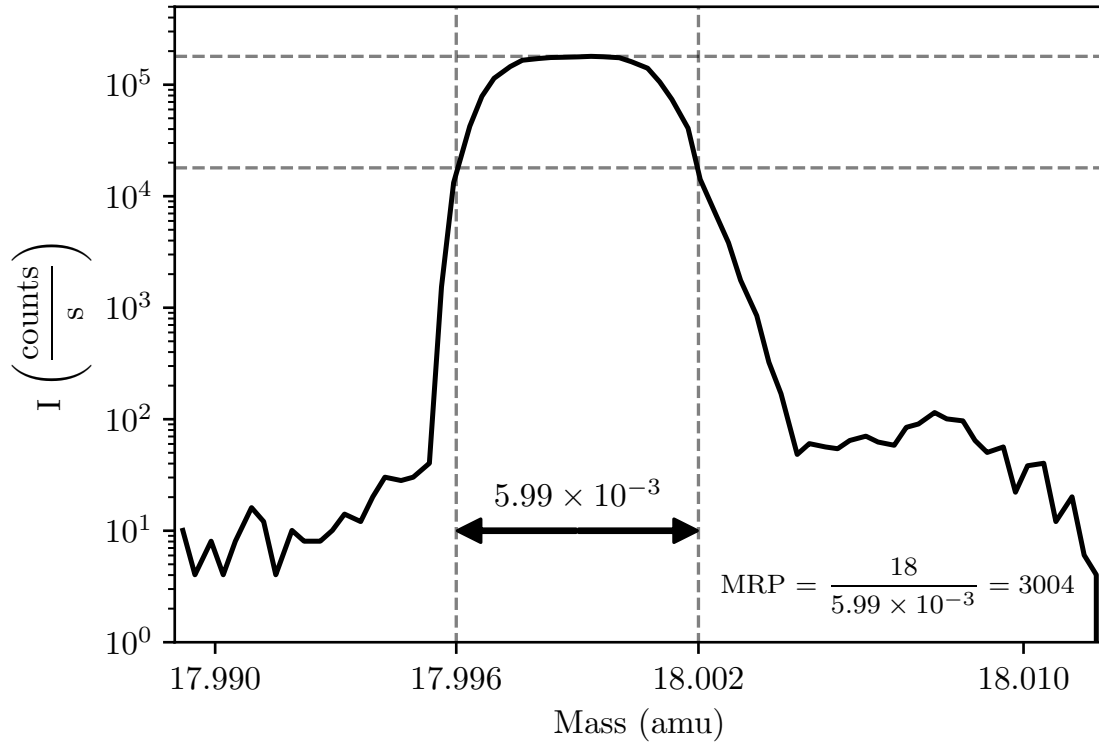
$^{18}\text{O}^-$ Mass Spectrum

Figure 2.2: Mass spectrum of $^{18}\text{O}^-$ sputtered from silicate glass. Note the interference from $^{17}\text{OH}^-$ and possibly $^{16}\text{OH}_2^-$ at masses slightly heavier than $^{18}\text{O}^-$. Dashed lines show the width of the peak at 10% of the peak height. This width (Δm) is used to determine the mass resolving power as shown in the equation.

was moved to put the area of interest under the beam. Either the $750\,\mu\text{m}$ or $400\,\mu\text{m}$ field aperture was then inserted, allowing only ions from a $30\,\mu\text{m}$ or $15\,\mu\text{m}$ diameter circular area in the center of the crater into the mass spectrometer, and measuring the target began.

In each measurement, we began by cycling the magnet through each of the masses three times. This was done in order to make the hysteresis effects of shifting the magnetic field uniform. While this was happening, the primary beam was turned on so as to pre-sputter the sample. Then, we performed a mass calibration of the locations of each of the mass peaks. When a highly doped standard glass was being measured

the peak locations of all the elements would be adjusted to match the most intense peak (as multiple peaks might be present at a particular mass). On the much lower concentration standards and unknowns, we only adjusted the peak location for Si. All the other elements would not produce enough counts in the short calibration time to make a visible peak, but molecular ion peaks might still be visible. Thus the most highly doped standards were always analyzed first multiple times in order to ensure that the mass peaks were in the correct locations and not shifting due to hysteresis. After calibrating the mass peaks, we then ran the analysis routine. This was set to use a 30 μm raster and perform 20 measurements of each species. The counting time for each measurement was variable based on the abundance of the species, with ^{28}Si being measured for 1s, ^{32}S being measured for 2.5s, and ^{65}Cu, ^{75}As, ^{80}Se, ^{81}Br, ^{121}Sb, and ^{130}Te being measured for 5s.

2.2.2 Standards

In order to develop and test combining high MRP and energy filtering, we applied the technique to glasses of known composition. A mount was assembled using an aluminum disk with several holes drilled through it as a base. Into each of these holes a grain of standard glass was placed, and the hole was filled with epoxy. The surface of the disk was then polished and gold coated. The standard glasses included were NIST 610, NIST 612, NIST 614, GSE-1G, GSD-1G, and GSA-1G. The mount also contains a grain of the cathodoluminescent mineral benitoite for the purpose of electron gun alignment as described in the SIMS procedure. The NIST glasses were chosen as they are soda-lime glasses similar in composition to rhyolites (Jochum *et al.*, 2011). NIST 610, 612, and 614 are doped with roughly 400, 40, and 1 μg/g respectively of a wide range of elements including all the chalcophiles we are interested in (Jochum

et al., 2011). These glasses have been well studied using a variety of techniques, and precise concentration measurements are available for almost all of the chalcophiles (Jochum *et al.*, 2011; Marks *et al.*, 2017; Wang and Becker, 2014). The literature concentration values and errors used for each of the NIST glasses are listed in table 2.2. Of note, the data presented by Jochum *et al.* (2011) includes estimates of the 95% confidence interval (CI) for different sample masses ranging from mg range to 0.02µg to account for compositional heterogeneity at small scales. Given that the diameter of the sampled area is at most 30 µm in the analyses described here and that the primary beam only sputters a few µm deep, it would make the most sense to use the estimate for the smallest mass. Most elements have almost the same 95% CI for all sample masses, with the exception of S and Se (Jochum *et al.*, 2011). These two have errors for the smallest sample mass that are a significant fraction of, or even exceed the concentration in the glass (Jochum *et al.*, 2011). For S we observe some degree of scatter between individual SIMS measurements of the glasses and a lack of co-linearity between 610, 612, and 614 when constructing the calibration curves, but not nearly to the degree suggested by the 95% CI for the lowest sample mass. For Se, there is almost no scatter and the curves are co-linear. This suggests that the 95% CI for the lowest mass is greatly exaggerated in these two cases. Therefore, for S we have elected to use the 95% CI for 0.1 µg for 610, 1 µg for 612, and 1 mg for 614. Likewise, for Se we used the 95% CI for the next highest mass (0.1, 0.1, and 1 µg) for all three glasses. Additionally, Jochum *et al.* (2011) gives significant concentrations of Br for the NIST glasses, with 610 having 93µg/g. This led us to believe the NIST glasses would be suitable for calibrating Br. We found that counts of Br in these glasses were extremely low, the three NIST glasses were not co-linear on the calibration curve plot, and the curve constructed gave suspiciously high Br for any unknown. Further research found sub-µg/g values for 610 and 612 published

in the literature for that much better lined up with our observations (Marks *et al.*, 2017). This meant that the NIST standards are not suitable for calibrating Br, but we kept it in our analysis routine for the sake of consistency and the fact that we can still qualitatively compare the Br/Si ion ratios between unknowns in the same session.

Table 2.2: Elemental Concentrations of the NIST Glasses

	NIST 610		NIST 612		NIST 614	
	µg/g	95% C.I	µg/g	95% C.I	µg/g	95% C.I
SiO2 (wt.%)	69.7	0.5	72.1	0.6	72.1	0.9
S	575	44	377	85	291	66
Cu	441	15	37.8	16.3	1.37	1.57
As	325	18	35.7	5.5	0.74	0.23
Se	138	43	16.3	7.8	0.40	0.24
Br	0.24[1]	0.06[1]	0.39[1]	0.02[1]	-	-
Sb	396	19	34.7	1.8	0.79	0.064
Te	302	-	30.9 [2]	-	-	-

Unless otherwise noted, values taken from Jochum *et al.* (2011). A dash denotes no value is available from the literature.

[1] - Marks *et al.* (2017)

[2] - Wang and Becker (2014)

The GS*-1G glasses are similar, but are made from basalt rather than soda-lime glass (Jochum *et al.*, 2005). GSE, GSD, and GSA have been doped with approximately 500, 50, and < 0.01 µg/g respectively of a wide range of elements (Jochum *et al.*, 2005). These glasses have also been well studied and precise measurements of most of the chalcophiles are available (Jochum *et al.*, 2005; Guillong *et al.*, 2005).

Elemental Concentrations of the GS*-1G Glasses

	GSE-1G		GSD-1G		GSC-1G		GSA-1G	
	µg/g	95% C.I	µg/g	95% C.I	µg/g	95% C.I	µg/g	95% C.I
SiO2 (wt.%)	52.9	0.4	52.5	1	53	0.4	51.5	0.4
S	-	-	-	-	-	-	-	-
Cu	349	40	40.0	1.4	19.5	1	2.3	0.4
As	290	-	30	-	4	-	0.54	-
Se[1]	20	50	1.9	4	0.2	0.4	-	-
Br[2]	281	32	31.9	0.02	-	-	-	-
Sb	444	34	44.5	1	5.7	0.6	8	0.2
Te	-	-	-	-	-	-	-	-

Table 2.3: Unless otherwise noted, values taken from Jochum *et al.* (2005). A dash denotes no value is available from the literature.
[1] - Guillong *et al.* (2005)
[2] - Marks *et al.* (2017)

However, we could find no measurements in the literature of either sulfur or tellurium for any of the GS glasses. The concentration values we used for the GS glasses are listed in table 2.3. As the two sets of standard glasses are at opposite ends of the chemical spectrum of igneous rocks, they allowed us to test how well our technique removes and separates molecular ions produced by alkaline vs mafic matricies. Additionally, since the NIST glasses are rhyolite-like they are suitable to use in calibrating our measurements of the Bandelier melt inclusions.

2.2.3 Analytical Sessions

In order to develop and prove our technique, we measured our two sets of standard glasses in seven different analytical sessions. In the first of these, we took mass spectra of ^{32}S, ^{65}Cu, ^{75}As, ^{121}Sb, ^{123}Sb, ^{128}Te, and ^{130}Te in NIST 610 and GSE with different combinations of energy filtering and MRP in order to determine what combination appeared to work best and which isotopes suffered the fewest interferences. NIST 610 and GSE were used since they contains high levels of all the elements. This ensured all the mass peaks were still easily visible even though the application of energy filtering and high MRP reduced count rates. Effectiveness of the energy filtering and MRP settings were then determined qualitatively by examining the mass spectra and looking for asymmetry in the mass peak that might represent overlap with the peak of a molecular ion. It was found that ^{121}Sb and ^{130}Te were the best isotopes to use. ^{65}Cu was chosen based on previous experience of the more common ^{63}Cu having worse interferences. ^{80}Se was chosen as it is the most abundant isotope. The stable isotope of As, at mass/charge $= 75$ was used. The MRP and energy filtering settings used for this work were recorded as degrees of rotations of the control knobs to used constrict the entrance and exit slits and rotations of the dials used to translate and constrict the energy window.

The second session attempted to measure these elements in the two sets of standard glasses. We roughly followed the SIMS procedure outlined in the preceding section, but we were less cautious and attempted to re-locate the mass peaks when analyzing the less concentrated glasses. These data were discarded as we accidentally measured molecular ions adjacent to the elemental ion peaks for several elements. For the third session, we added ^{80}Se and ^{81}Br to our routine and again attempted to measure the two sets of glasses. These data had to be discarded as well, as it was

discovered that NIST 610 and GSD were becoming electrically charged, destabilizing count rates and making the data produced useless. Examination of the sample mount revealed that the epoxy plugs containing the glass grains had shrunk, breaking the electrical connection between the gold coat and the surrounding aluminum disk. Additionally, the gold coat on some of the grains had become damaged due to improper handling. To mitigate these issues, multiple dots of conductive carbon paint were applied to the aluminum-epoxy boundary and epoxy-grain boundary of each standard to ensure electrical conductivity.

In the next session, we quantified the degree of energy filtering being used. To do this, we collected energy spectra of the molecular ion $^{27}Al_3^-$ which has a narrow and mostly symmetric energy spectrum ideal for measuring the energy window's bandpass and offset. We collected three spectra under different conditions; one with the energy window centered and the width of the slits set to the same as had been used before, one with it translated by the number of turns determined earlier with the same slit width, and one with it translated by the same amount and the slits closed farther down. The three energy spectra produced are summarized in figure 2.1. From these three spectra, we were able to determine the energy window settings we had found to be ideal represented a $-27\,\mathrm{V}$ offset with a $40\,\mathrm{eV}$ bandpass. Additionally, in the same session we made measurements of the background noise in the electron multiplier detector by performing an analysis of mass 2.5 (for which no ion of the correct mass/charge ratio exists).

The fifth analysis session primarily examined the GS*-1G glasses with the repaired standard mount. Three analyses of NIST 610 were also made for comparison to the GS glasses. During the first two analyses of the NIST glass it was noted that the count rates of Si were rapidly declining (a sign of charging), and for the third analysis care was taken to select a better spot on the NIST glass away from any damaged por-

tion of the gold coat and near one of the spots of conductive paint. This analysis had steady counts and was the only one we used. Each of the GS glasses was measured twice, with the exception of GSA which was only measured once.

The sixth session took place over three days, with the first two being dedicated to measuring the standard glasses, and the third to measuring the Bandelier melt inclusions as will be discussed in chapter 3. The first day was primarily dedicated to carefully setting up the instrument as described in the proceeding section on the SIMS analysis procedure. Analyses of the NIST glasses were also made that day with four measurements of 610, two of 612, and one of 614. The instrument was kept running overnight, only shutting down the Cs^+ source in the hopes that the factors determining the relative sputter yield and slope of the calibration curve would not change. The next day, one more measurement of each of the NIST glasses was made and it was found that the count ratios were within error of those taken the previous day. Each NIST and GS glass was then analyzed twice with just 3000 MRP to determine how the energy filtering approach was reducing the molecular background. In these analyses, we accidentally calibrated the instrument to measure a molecular ion peak instead the peak of Sb, so the Sb data had to be discarded. We then attempted to measure the GS glasses with both energy filtering and high MRP, but we only managed to perform two analyses of GSE and one of GSD before a software crash forced us to reboot the whole instrument.

The seventh session focused heavily on the GS glasses, measuring them in both our standard mount and another mount labelled "Guggino" that also contained GSC-1G intermediate in composition between GSD and GSA. Each NIST and GS glass was analyzed twice or more in our mount. In the other mount, multiple measurements of GSE, GSD, and GSC were made as well as a single measurement of NIST 610.

2.3 Results

From the count rates obtained from each analysis we created calibration curves for each element. These curves plot count rate of the ion multiplied by the weight percent Si in the sample and divided by the count rate of ^{28}Si$^-$ versus the independently determined µg/g concentration of the element in the sample. These are shown in figures 2.3-2.15. The figures clearly show that the relationship between normalized count ratios and concentration remains linear when applying both MRP and energy filtering. The error bars in the figures represent two standard deviations or the 95% confidence level for the concentration as provided by the literature on the horizontal axis, and the vertical axis represents two standard errors of the mean in our normalized count ratios assuming no error in the weight percent SiO$_2$. We chose to use the standard error of the mean rather than the standard deviation as we are interested in what the true mean ion ratio is, and not how much scatter there is in the count rates over the course of the analysis. As our count rates for the trace chalcophiles are extremely low, in the range of a few counts/s, there is quite a bit of random scatter in the count rate and ion ratios over the course of each analysis. This leads to very large standard deviations that overstate the error to which we know the mean ion ratios during the analysis. Therefore, the standard error of the mean is a more appropriate measurement of the error.

In the calibration curves, the relationship between normalized count rate and concentration should be linear and the regression line through the standards can be used to derive concentration of the element in an unknown from its normalized count rate. In our case, we will be using these lines to evaluate the quality of our data and the molecular ion "background" still present after energy filtering and high MRP have been applied. In the ideal case with no background the regression line should inter-

cept the origin; that is, when there is exactly $0\,\mu\mathrm{g/g}$ of an element in a sample, there are no counts recorded. If a signal is still detected, then that is an indicator that the technique has not completely removed all interferences.

We will start by assuming any interference is the same for all the glasses, implying the interference comes from the major element chemistry and is not dependent on the level of doped elements in each glass. The presence of such a uniform interference shifts the entire curve upward, giving it a positive y-intercept. Ideally, if the calibration curve were perfectly constrained then this intercept would give the count rate of the molecular ion, and shifting the curve down to the intercept and evaluating the count ratio on the new curve would give the background "concentration" of the molecular ion. However due to heterogeneity in the glasses, errors in the measurements of the count ratios, and errors in the concentration values given by the literature the y-intercept can shift substantially, even becoming negative in many cases. Thus, rather than try to obtain an exact value for the background concentration accounting for all possible errors, we used an approach to make reasonable estimates of the background. This was done by first creating a new calibration curve using a least squares fit of $y = ax$ to the data, forcing it through the origin. As the NIST 610 and GSE data points are far from the origin and the background is comparatively small, the difference in slope between the curve obtained by normal linear regression and the origin-forced line will be small. For the glasses with concentrations close to 0, the difference between the literature value for the concentration and the value obtained by applying the count rate to the origin forced curve is approximately equal to the background concentration. The backgrounds calculated in this way are presented in tables 2.6, 2.7, 2.8, and 2.9, and these are summarized in tables 2.4 and 2.5.

Tables 2.6 and 2.7 show data from the sixth analysis session where data was col-

NIST Molecular Ion Background Summary

	Without Filtering	With Filtering		
		6th Session	7th Session	Average
Cu	6.0	4.5	6.7	6.0
As	2.7	0.3	0.5	0.4
Se	0.5	0.6	1.3	1.0
Sb	-	1.1	0.6	0.9
Te	0.8	1.1	0.9	1.0

Table 2.4: Averages of the background concentration estimates in the NIST glasses from tables 2.6 and 2.8. All values are in µg/g.

GS*-1G Molecular Ion Background Summary

	Without Filtering	With Filtering		
		GSA	GSC	Average
Cu	1.1	6.9	-	6.9
As	6.5	4.0	1.0	2.5
Se	3.0	5.5	5.4	5.4
Br	0.7	1.3	-	1.3
Sb	-	0.5	0.4	0.4

Table 2.5: Summary of the background concentration estimates in the GS*-1G glasses from tables 2.7 and 2.9. All values are in µg/g. The GSC value for Cu is excluded due to it having much greater than $0\,\mathrm{µg/g}$ Cu. The GSC Br value is also excluded due to not having a reference concentration value, and the background obtained is much higher than from GSA implying that we cannot assume 0 Br in GSC. The Se value is included for GSC despite not having a reference concentration however, as both GSA and GSC give almost identical backgrounds implying they both have approximately $0\,\mathrm{µg/g}$ Se.

lected with and without energy filtering. Antimony data from the no energy filtering analyses during this session had to be discarded due to measuring the wrong mass peak. Additionally, no estimates of the background with energy filtering for the GS glasses could be made as the instrument crashed before obtaining measurements of GSA with these settings. The seventh session (tables 2.8, 2.9, and 2.10) only con-

tains data taken with energy filtering. This session made measurements of the GS glasses on two separate mounts, the mount we constructed and the Guggino mount mentioned earlier. As we did not measure GSA on the Guggino mount, GSC was used to estimate the background. Errors were estimated based solely off the count ratio standard error of the mean, assuming no error in the slope of the calibration curve and no error in the literature concentration value of the glass

From these tables, we can see that our backgrounds are around $1\,\mu g/g$ for most elements in the NIST glasses and range from 0.5 to $7\,\mu g/g$ for the GS*-1G glasses. By adding energy filtering to 3000 MRP, we do not remove any background counts in most cases. In fact, it appears the backgrounds are slightly worse when comparing the data taken with energy filtering to the data taken without it. This can be explained by the fact that adding energy filtering apparently reduces the count rate of the chalcophile ions faster than the normalizing Si, decreasing the slope of the calibration curve and increasing the effects of count rate errors on the calculated concentrations. Another possible contribution is that decreasing the number of counts by applying energy filtering increases the importance of the electron multiplier noise. Our measurements of mass 2.5 during the third analysis session showed an average background count rate of 0.05 counts/s. During the sixth analysis session, count rates of Sb and Te were in the 10's to 1's counts/s in NIST 614 without energy filtering, but with it applied the count rates dropped to around 0.5 counts/s on average. In this case, the background from the electron multiplier noise constitutes 10% of our counts. This is not enough to completely offset a significant reduction in molecular ion counts, but it is enough that if we aren't successfully filtering any molecular ion out then it will appear we have worse backgrounds than without filtering. Additionally, the calculated backgrounds for NIST vary significantly between individual sessions, for example the Se background estimate more than doubled between the

two sessions while the Sb background was halved. These variations are greater than our estimate of error based on the 2 standard errors of the mean. The GS glasses also show significant variation between the background from GSA on our mount and GSC in the Guggino mount obtained in the same session, likely simply due to using different standards to estimate the error.

While our estimates of the background are quite variable for the measurements made between multiple analysis sessions, the averages of the backgrounds using energy filtering are within error of those made without energy filtering. The variability may in part be due to the fact we ignored uncertainties in the concentrations of the chalcophiles in these glasses provided by the literature to simplify our error estimates. Additionally, any inhomogeneity in the glasses at small scales could change the background estimate significantly. If a particular element was inhomogeneous, one might expect to see significant scatter in the M^-/Si^- ratios between measurements. While this is true of the most heavily doped glasses, individual measurements of the least doped glasses NIST 614 and GSA are usually within error of each other. This could be explained by the fact that multiple measurements of the same glass in a single session almost always measured two points in very close proximity. If the glass were inhomogeneous at the scale of 100's of µm, we would not see much scatter in a single analysis session, but between analysis sessions sampling different areas of the glass could produce significantly different results.

One major outlier is As, for which the background estimate in the NIST glasses obtained using only MRP is almost 7 times higher at $2.7\,\mu g/g$ compared to the $0.4\,\mu g/g$ background from both session's energy filtering data. For the GS glasses, energy filtering also reduces the As background, but it is not clear by how much. If one looks at the data for GSA it appears that the background was only reduced from 6 to $4\,\mu g/g$, but if we instead use the GSC data it appears to have been reduced down

25

to $1 \, \mu g/g$. This suggests that either the literature value for the As concentration in GSC is too high, which would make the background appear better than it really is, or the concentration in GSA is too low making the background appear worse.

Additionally, comparing the calibration curves from the seventh session of the NIST and GS glasses in our mount shows how strong the differences in matrix effects are for these elements between rhyolites and basalts. The ratio of the slope of the GS curve to the slope of the NIST curve ranges from 1.3 for Sb to 1.6 for As, with a single outlier being Se for which the ratio is 0.3.

2.4 Conclusions

In most situations, combining high MRP with energy filtering is not useful. While our data show that this combination does not negatively effect the linear relationship between normalized count ratios and concentration, adding the ~ 27 eV of energy filtering in this study reduces count ratios by 2 to 5 times but does not visibly reduce the apparent background concentration. Thus it would seem that applying both energy filtering and high MRP is counterproductive.

However, there is a single outlier. When applying energy filtering, Arsenic backgrounds were decreased by almost sevenfold in the NIST glasses down to $\sim 0.4 \, \mu g/g$ at the cost of reducing the count rate by a factor of 4. Similarly, in the GS glasses there was a decrease in the background concentration by a factor somewhere in the range of 1.5 to 6. Such a large decrease in background could outweigh the reduction in counts in cases where ppm to sub-ppm levels of As are expected. Thus this technique seems to still have the potential to be useful for specific elements. However, we cannot say if the combination of high MRP and energy filtering is necessary for As. It may be that running at low MRP with energy filtering may be enough to remove the molecular ions interfering with As in samples with more than a few $\mu g/g$. Fur-

ther experimentation analyzing As with just energy filtering would be necessary to determine this. If this technique is in fact helpful for As, there may be other elements that would benefit from it. This would have to be experimentally determined on an element-by-element basis for a given matrix.

However, applying this technique to elements which mostly form positive ions may prove problematic. When analyzing negative ions, we mostly only need to worry about singly charged molecular interferences as many multiply charged negative ions are unstable. When analyzing positive ions, it is possible to also have multiply charged ions interfere with the species of interest, introducing more interferences which energy filtering might be effective or ineffective against. An example is the measurement of carbon in mafic silicate glasses. The Edinburgh SIMS lab uses positive secondary ions, but must remove the interference from $^{24}Mg^{2+}$ on $^{12}C^+$ using high mass resolution. They also apply energy filtering to this signal, with good results (J. Craven, Edinburgh, personal communication).

In this study, combining energy filtering with high MRP does little other than reduce ion counts. There is one specific case with As where it appears beneficial but it has yet to be determined if the same results could be achieved by energy filtering alone. Assuming the combination is in fact beneficial for As, there may be other elements which could also benefit. However, given the number of elements we studied it seems likely that that there will be very few cases where it makes enough of a difference to be beneficial, and it may only work for elements which form negative ions where there are fewer potential interfering species. Thus, it seems energy filtering is best used alone without significant MRP, as has been successfully demonstrated by Shimizu and Hart (1982) in the study of positive secondary ions from Sr to U.

Session 6 NIST Molecular Ion Backgrounds with and without Energy Filtering

	Known Conc.	With Energy Filtering			Without Energy Filtering		
		Analysis	Measured	Background	Analysis	Measured	Background
Cu	1.37	1	5.6±1.5	4.2±1.5	1	7.2±1.8	5.8±1.8
		2	6.1±1.1	4.8±1.1	2	7.6±1.6	6.3±1.6
		Average	5.8±0.9	4.48±0.9	Average	7.4±1.2	6.0±1.2
As	0.74	1	1.4±0.3	0.7±0.3	1	3.5±0.2	2.7±0.2
		2	0.7±0.2	-0.1±0.2	2	3.5±0.2	2.7±0.2
		Average	1.1±0.2	0.31±0.2	Average	3.5±0.1	2.7±0.1
Se	0.40	1	0.8±0.2	0.4±0.2	1	0.9±0.0	0.5±0.0
		2	1.1±0.2	0.7±0.2	2	0.9±0.1	0.5±0.1
		Average	1.0±0.1	0.57±0.1	Average	0.9±0.0	0.5±0.0
Sb	0.79	1	2.2±0.4	1.4±0.4	1	498.2±13.5	497.4±13.5
		2	1.6±0.5	0.8±0.5	2	535.8±3.6	535.0±3.6
		Average	1.9±0.3	1.12±0.3	Average	517.0±7.0	516.2±7.0
Te	0.00	1	1.2±0.4	1.2±0.4	1	0.8±0.1	0.8±0.1
		2	0.9±0.3	0.9±0.3	2	0.8±0.1	0.8±0.1
		Average	1.1±0.3	1.07±0.3	Average	0.8±0.04	0.8±0.04

Table 2.6: Estimates of the background concentrations in the NIST glasses calculated from analysis session 6's data. Data presented in the table is of NIST 614, and all values are in µg/g. The "Known Conc." column contains the independently determined concentrations of each element in NIST 614 from Table 2.2. If no concentration value is available, it is assumed to be 0. Four measurements of NIST 614 were made, two with energy filtering and two without. The data for each of these analyses is presented, as well as the average of each pair. The "Measured" column contains the concentration in NIST 614 determined by dividing the count ratio by the slope of the origin-forced calibration curve. The "Background" column contains the estimate of the molecular ion background obtained by subtracting the known concentration from the measured. No data for Sb without energy filtering is available due to the wrong peak having been targeted during those analyses.

Session 6: GS*-1G Molecular Ion Backgrounds Without Energy Filtering

	Known Conc.	Measured Conc.	Background
Cu	2.20	3.3±0.3	1.1±0.3
As	0.54	7.0±0.2	6.5±0.2
Se	0.00	3.0±0.1	3.0±0.1
Br	0.00	0.7±0.03	0.7±0.03

Table 2.7: Estimates of the background concentration from molecular ion interferences in the GS glasses based on the sixth analysis session's data. All values are in units of µg/g, and the errors represent 2 standard deviations of the mean assuming there are no errors in the slope of the calibration curve. All data presented was obtained without the use of energy filtering. Due to instrumental failure, no measurements of GSA were obtained with energy filtering during this session. The column labeled "Known Conc." is the independently measured chalcophile concentrations in GSA (see Table 2.3). If no independent measurement exists for an element in GSA, it is assumed to be 0. The "Measured Conc." column contains the concentration of the element in GSA obtained by dividing the normalized count ratio by the slope of the origin-forced calibration curve. The "Background" column contains an estimate of the background obtained by subtracting the measured concentration from the known concentration.

Session 7 NIST Molecular Ion Backgrounds

	Known Conc.	Analysis	Measured	Background
Cu	1.37	1	9.77±3.5	8.4±3.5
		2	6.4±2.1	5.0±2.1
		Average	8.1±2.0	6.7±2.0
As	0.74	1	1.14±0.4	0.4±0.4
		2	1.3±0.4	0.6±0.4
		Average	1.2±0.3	0.5±0.3
Se	0.40	1	1.99±0.5	1.6±0.5
		2	1.5±0.2	1.1±0.2
		Average	1.7±0.3	1.3±0.3
Sb	0.79	1	1.26±0.8	0.5±0.8
		2	1.5±0.9	0.8±0.9
		Average	1.4±0.6	0.6±0.6
Te	0.00	1	0.72±0.4	0.7±0.4
		2	1.0±0.4	1.0±0.4
		Average	0.9±0.3	0.9±0.3

Table 2.8: Estimates of the background concentrations in the NIST glasses calculated from analysis session 7's data. Data presented in the table is of NIST 614, and all values are in μg/g. Errors represent 2 standard errors of the mean, calculated assuming no error in the slope of the calibration curve. The "Known Conc." column contains the independently determined concentrations of each element in NIST 614 from Table 2.2. If no concentration value is available, it is assumed to be 0. Two measurements of NIST 614 were made, and data for each of these analyses is presented as well as the average of the two. The "Measured" column contains the concentration in NIST 614 determined by dividing the count ratio by the slope of the origin-forced calibration curve. The "Background" column contains the estimate of the molecular ion background obtained by subtracting the known concentration from the measured one.

Session 7 GSA-1G Molecular Ion Backgrounds

	Known Conc.	GSA-1G		
		Analysis	Measured	Background
Cu	2.20	1	10.7±1.7	8.5±1.7
		2	7.6±1.8	5.4±1.8
		Average	9.1±1.2	6.9±1.2
As	0.54	1	4.2±0.6	3.7±0.6
		2	4.9±0.4	4.4±0.4
		Average	4.6±0.3	4.0±0.3
Se	0.00	1	6.1±0.8	6.1±0.8
		2	4.9±0.8	4.9±0.8
		Average	5.5±0.6	5.5±0.6
Br	0.00	1	1.5±0.3	1.5±0.3
		2	1.2±0.2	1.2±0.2
		Average	1.3±0.2	1.3±0.2
Sb	8.00	1	9.7±1.6	1.7±1.6
		2	7.3±1.1	-0.7±1.1
		Average	8.5±1.0	0.5±1.0

Table 2.9: Estimates of the background concentrations in the GS glasses calculated from analysis session 7's data. Data presented in the table is of GSA from our mount and all values are in μg/g. Errors represent 2 standard errors of the mean, calculated assuming no error in the slope of the calibration curve. The "Known Conc." column contains the independently determined concentrations of each element in GSA from Table 2.3. If no concentration value is available, it is assumed to be 0. Two measurements of GSA were made. The data for each of these analyses is presented, as well as the average. The "Measured" column contains the concentration in the glass determined by dividing the count ratio by the slope of the origin-forced calibration curve. The "Background" column contains the estimate of the molecular ion background obtained by subtracting the known concentration from the measured.

Session 7 GSC-1G Molecular Ion Backgrounds

	Known	GSC-1G		
	Conc.	Analysis	Measured	Background
Cu	19.50	1	17.2±3.2	-2.3±3.2
		2	16.3±3.5	-3.2±3.5
		Average	16.7±2.4	-2.8±2.4
As	4.00	1	5.0±0.7	1.0±0.7
		2	5.1±0.9	1.1±0.9
		Average	5.0±0.6	1.0±0.6
Se	0.20	1	6.1±1.4	5.9±1.4
		2	5.2±1.4	5.0±1.4
		Average	5.6±1.0	5.4±1.0
Br	0.00	1	3.7±0.6	3.7±0.6
		2	3.6±0.5	3.6±0.5
		Average	3.6±0.4	3.6±0.4
Sb	5.70	1	5.7±1.4	0.0±1.4
		2	6.4±1.2	0.7±1.2
		Average	6.1±0.9	0.4±0.9

Table 2.10: Estimates of the background concentrations in the GS glasses calculated from analysis session 7's data. Data presented in the table is of GSC in the "Guggino" mount and all values are in µg/g. Errors represent 2 standard errors of the mean, calculated assuming no error in the slope of the calibration curve. The "Known Conc." column contains the independently determined concentrations of each element in GSC from Table 2.3. If no concentration value is available, it is assumed to be 0. Two measurements of GSC were made. The data for each of these analyses is presented, as well as the average. The "Measured" column contains the concentration in the glass determined by dividing the count ratio by the slope of the origin-forced calibration curve. The "Background" column contains the estimate of the molecular ion background obtained by subtracting the known concentration from the measured.

Figure 2.3: Calibration curves forced through the origin of S and Cu in the NIST glasses from the 6th analysis session. The two curves were created from analyses made with (red) and without (green) energy filtering. Dashed lines in the inset show the projection of the count ratios of 614 on to the respective calibration curve, marking the concentration that would be calculated from the curve. Equations in red and green are of the calibration curves. Note that the NIST glasses are not suitable for calculating the S background as the lowest concentration glass contains much greater than $0\,\mu g/g$ of S. Additionally, the inhomogeneity of S at microscopic scales in NIST introduces large uncertainties and makes the calibration curve fit poorly to the data.

Figure 2.4: Calibration curves forced through the origin of As and Se in the NIST glasses from the 6th analysis session. The two curves were created from analyses made with (red) and without (green) energy filtering. Dashed lines in the insets show the projection of the count ratios of 614 on to the respective calibration curve, marking the concentration that would be calculated from the curve. Equations in red and green are of the calibration curves.
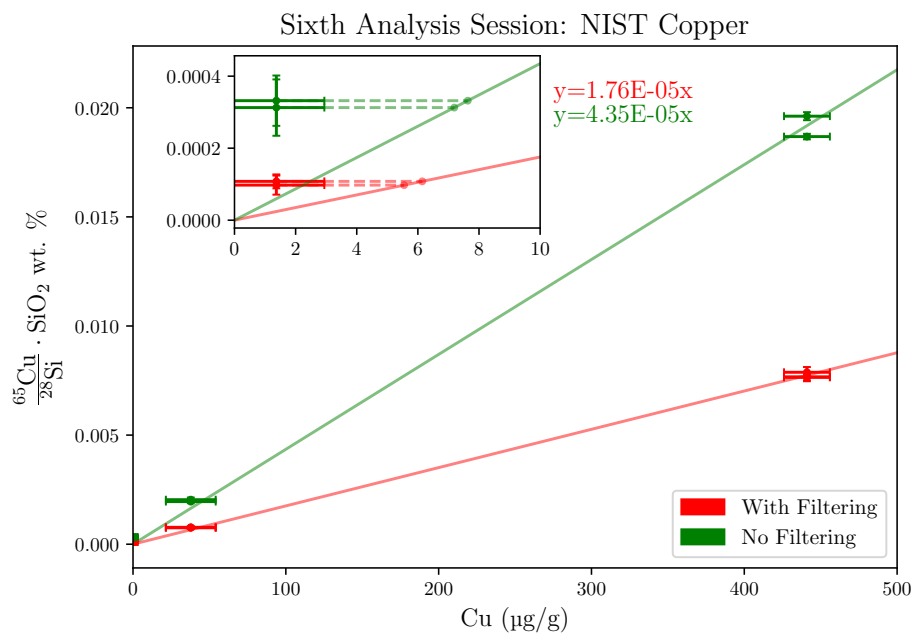
Figure 2.5: Calibration curves forced through the origin of Br and Sb in the NIST glasses from the 6th analysis session. The two curves were created from analyses made with (red) and without (green) energy filtering. The Sb plot only contains measurements made with energy filtering due to misplacing the Sb peak position during the analyses made with no energy filtering. Dashed lines in the insets show the projection of the count ratios of 614 on to the respective calibration curve, marking the concentration that would be calculated from the curve. Equations in red and green are of the calibration curves. Note that all the NIST glasses contain less than $1\,\mu g/g$ of Br, making the calibration curve essentially meaningless.
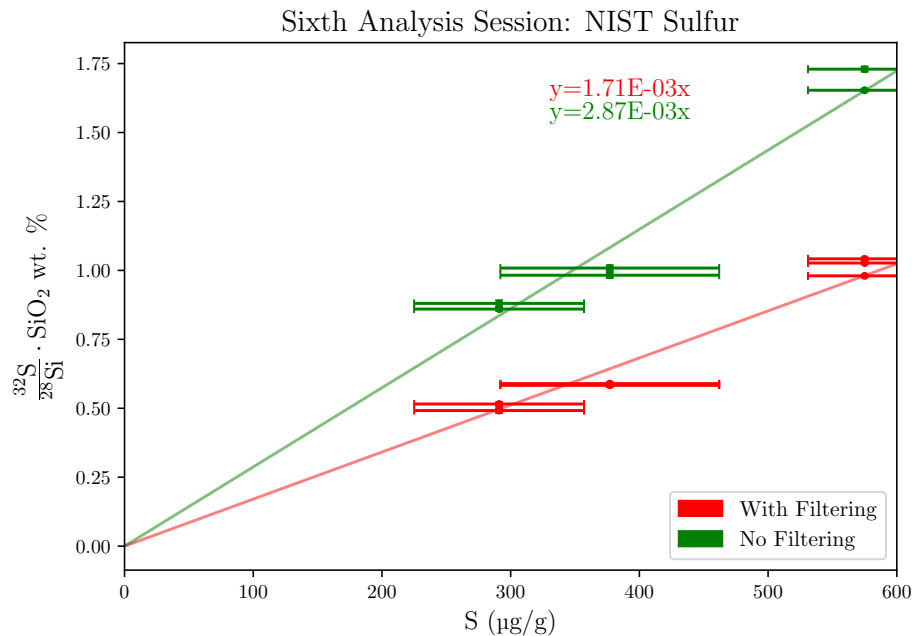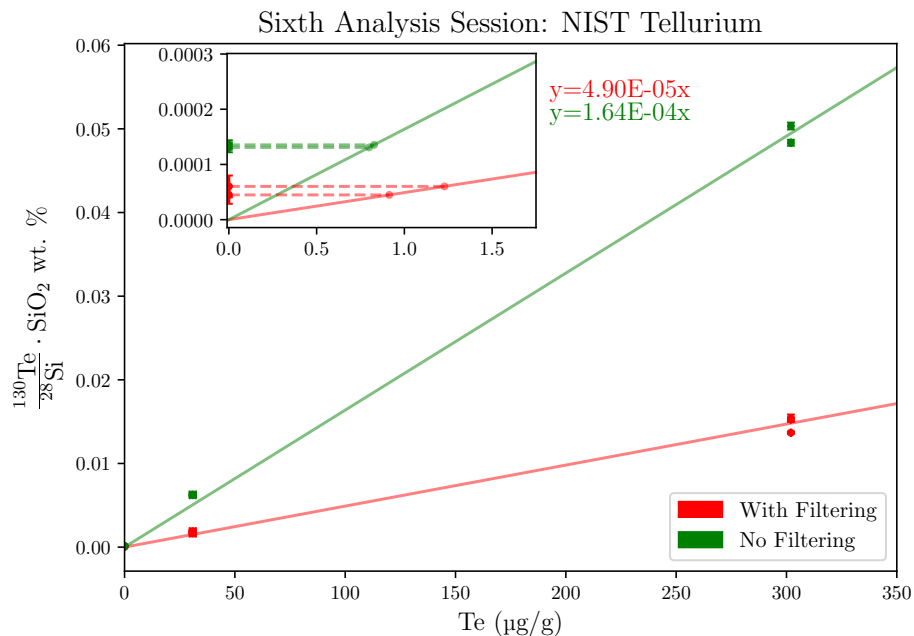
Figure 2.6: Calibration curves forced through the origin of Te in the NIST glasses from the 6th analysis session. The two curves were created from analyses made with (red) and without (green) energy filtering. Dashed lines in the inset show the projection of the count ratios of 614 on to the respective calibration curve, marking the concentration that would be calculated from the curve. Equations in red and green are of the calibration curves.
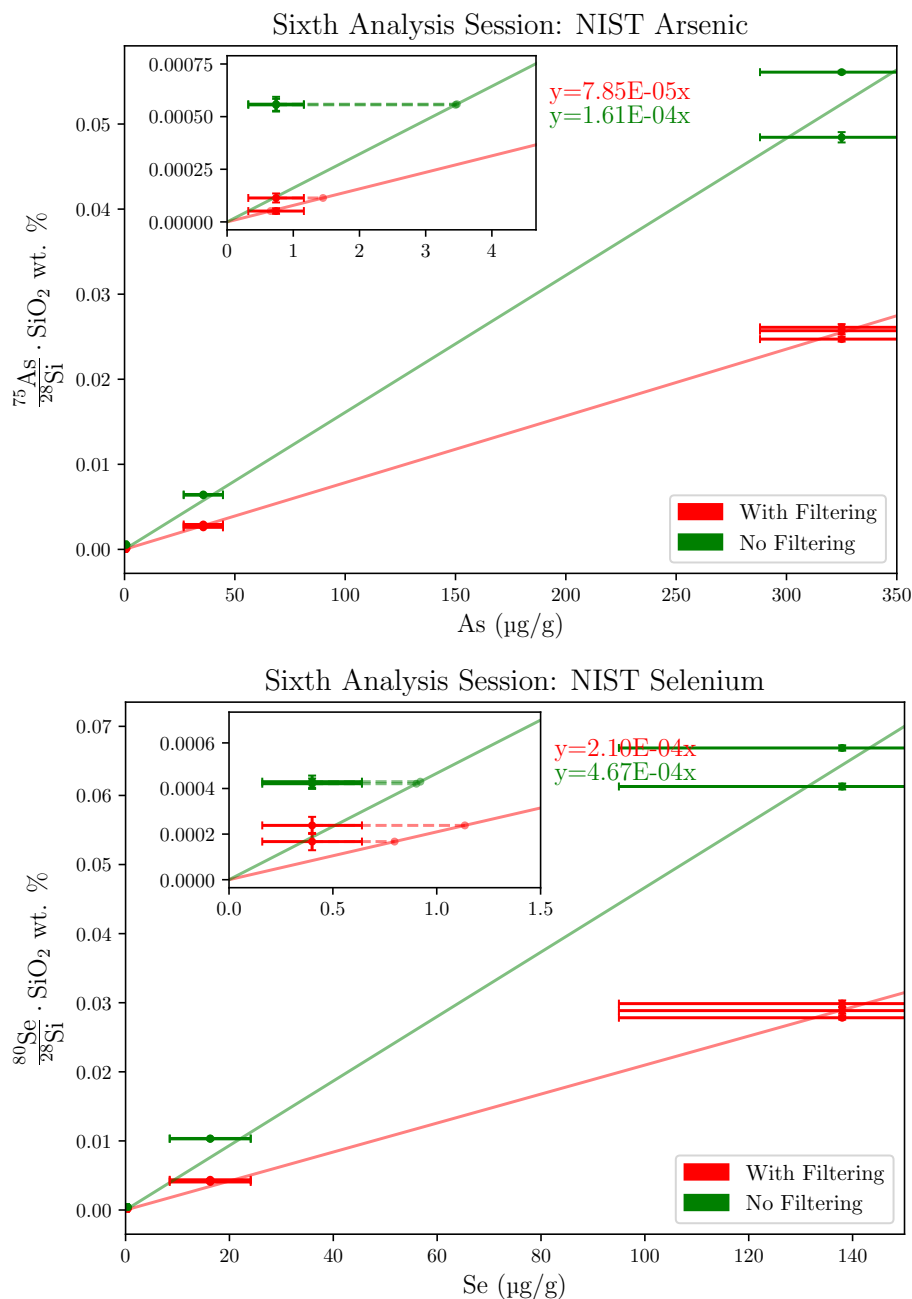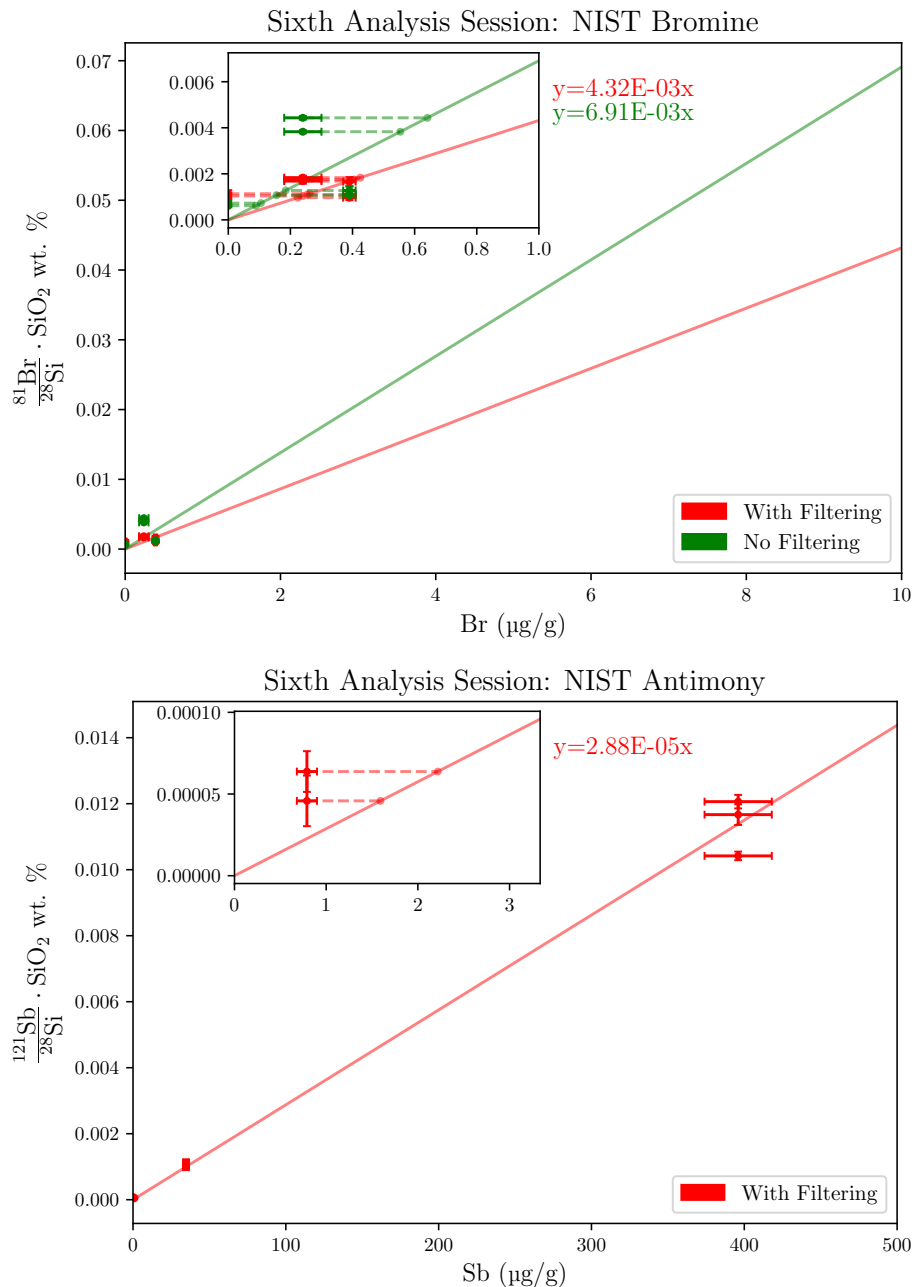
Figure 2.7: Calibration curves forced through the origin of Cu and As in the GS*-1G glasses from the 6th analysis session. The two curves were created from analyses made with (red) and without (green) energy filtering. No measurement of GSA was made with energy filtering in this session due to instrumental failure. Dashed lines in the insets show the projection of the count ratios of GSA on to the no energy filtering curve, marking the concentration that would be calculated from the curve. The equations in red and green are of the calibration curves.

Figure 2.8: Calibration curves forced through the origin of Se and Br in the GS*-1G glasses from the 6th analysis session. The two curves were created from analyses made with (red) and without (green) energy filtering. No measurement of GSA was made with energy filtering in this session due to instrumental failure. Dashed lines in the insets show the projection of the count ratios of GSA on to the no energy filtering curve, marking the concentration that would be calculated from that curve. The equations in red and green are of the calibration curves.
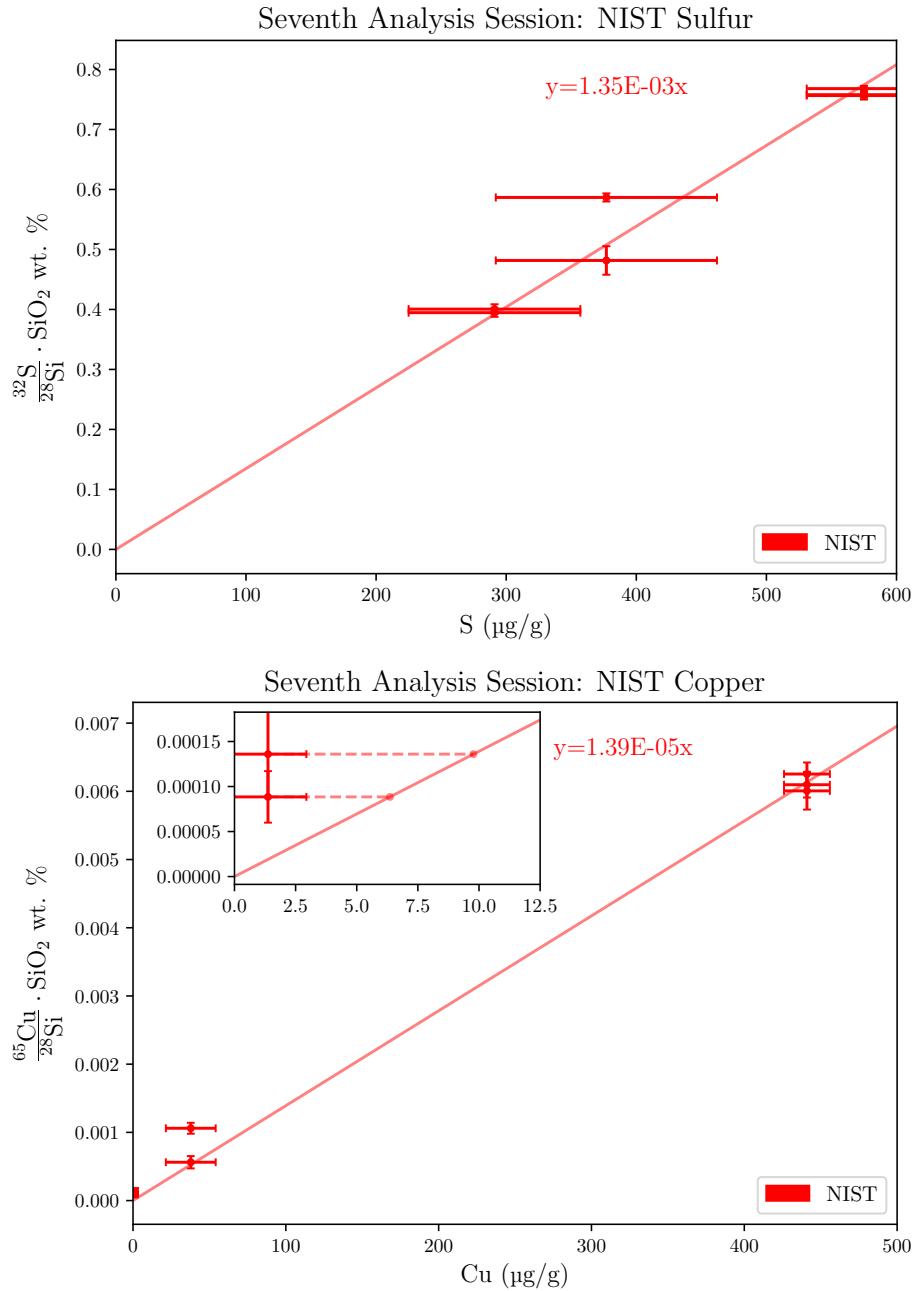
Figure 2.9: Calibration curves forced through the origin of S and Cu in the NIST glasses from the 7th analysis session. Dashed lines in the inset show the projection of the count ratios of 614 on to the calibration curve, marking the concentration that would be calculated from the curve. The equation is of the calibration curve. Note that the NIST glasses are not suitable for calculating the S background as the lowest concentration glass contains much greater than $0 \, \mu g/g$ of S. Additionally, the inhomogeneity of S at microscopic scales in NIST introduces large uncertainties and makes the calibration curve fit poorly to the data.
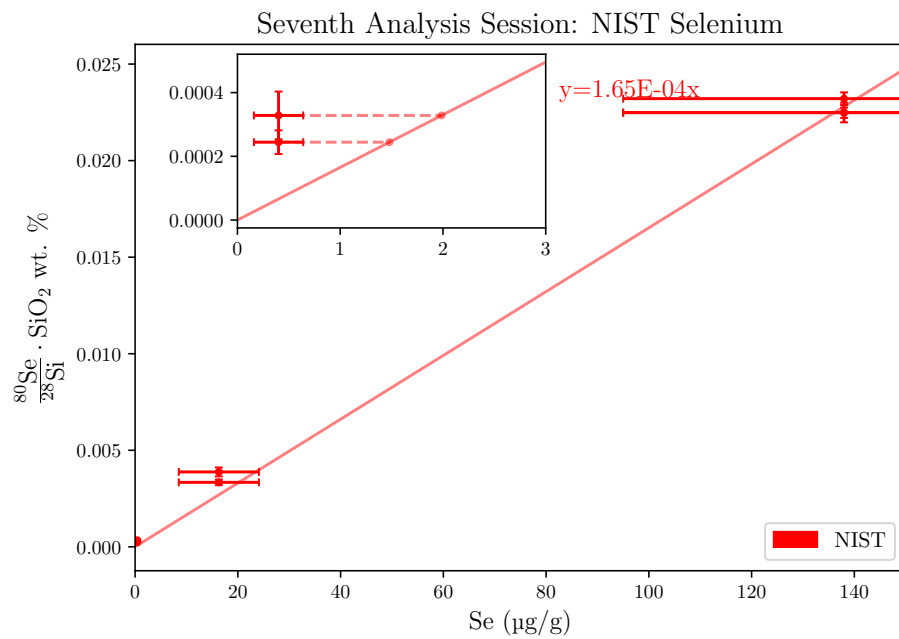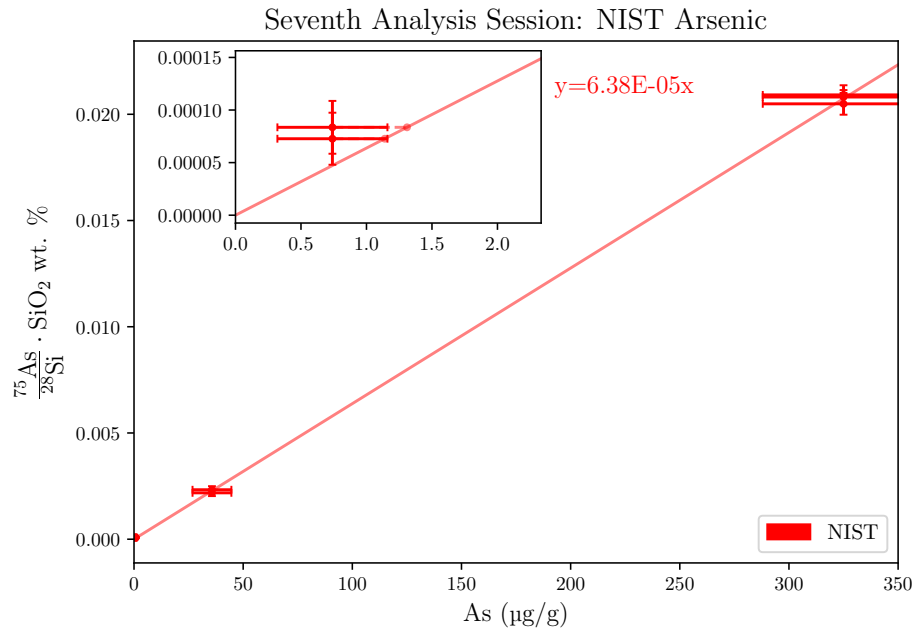
Figure 2.10: Calibration curves forced through the origin of As and Se in the NIST glasses from the 7th analysis session. Dashed lines in the insets show the projection of the count ratios of 614 on to the calibration curve, marking the concentration that would be calculated from the curve. The equation is of the calibration curve.
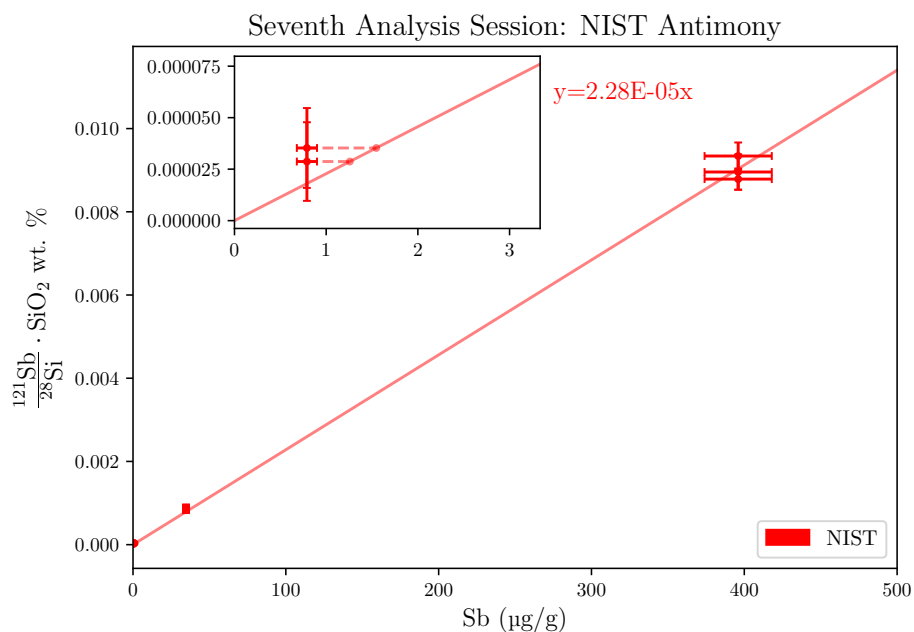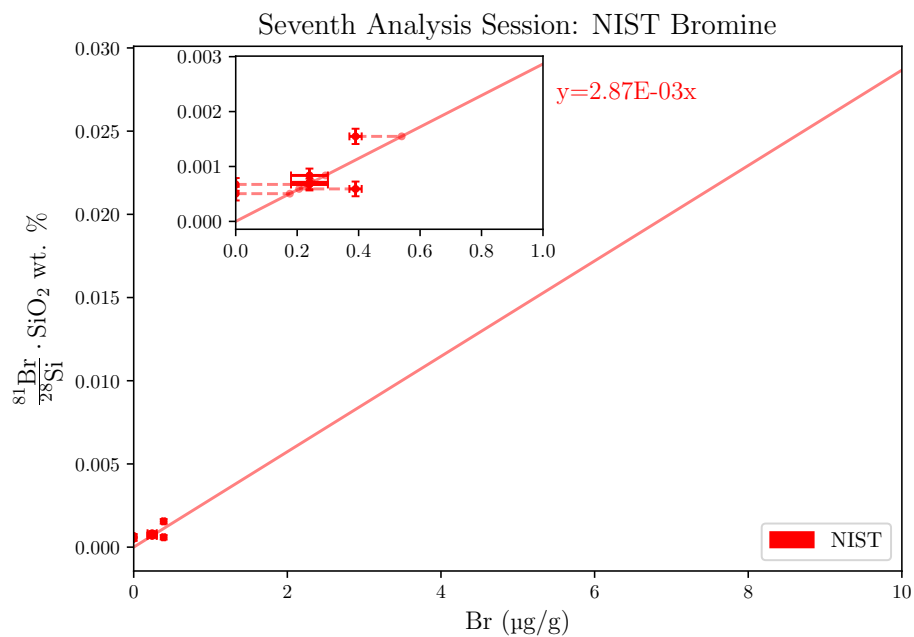
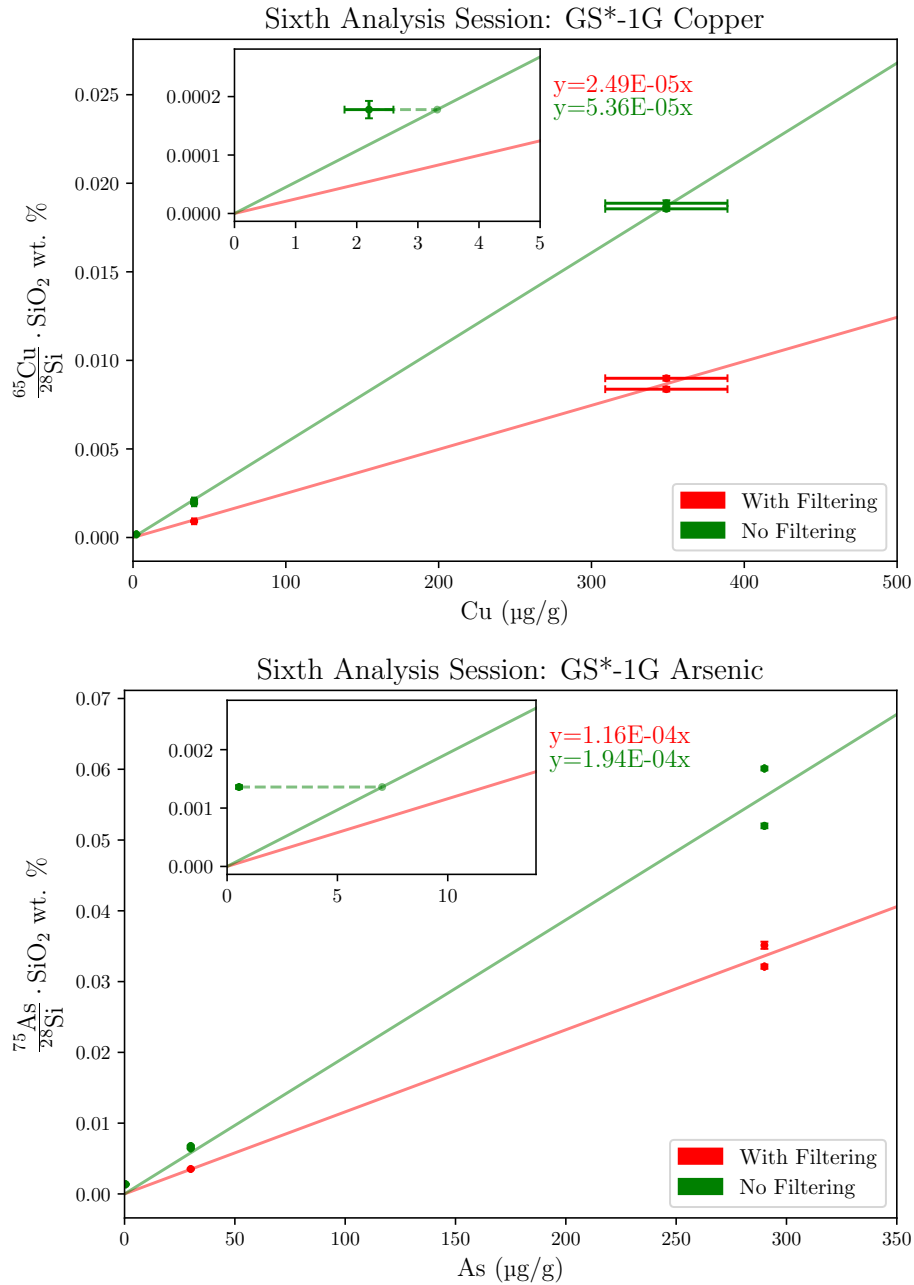Figure 2.11: Calibration curves forced through the origin of Br and Sb in the NIST glasses from the 7th analysis session. Dashed lines in the insets show the projection of the count ratios of 614 on to the calibration curve, marking the concentration that would be calculated from the curve. The equation is of the calibration curve.

41
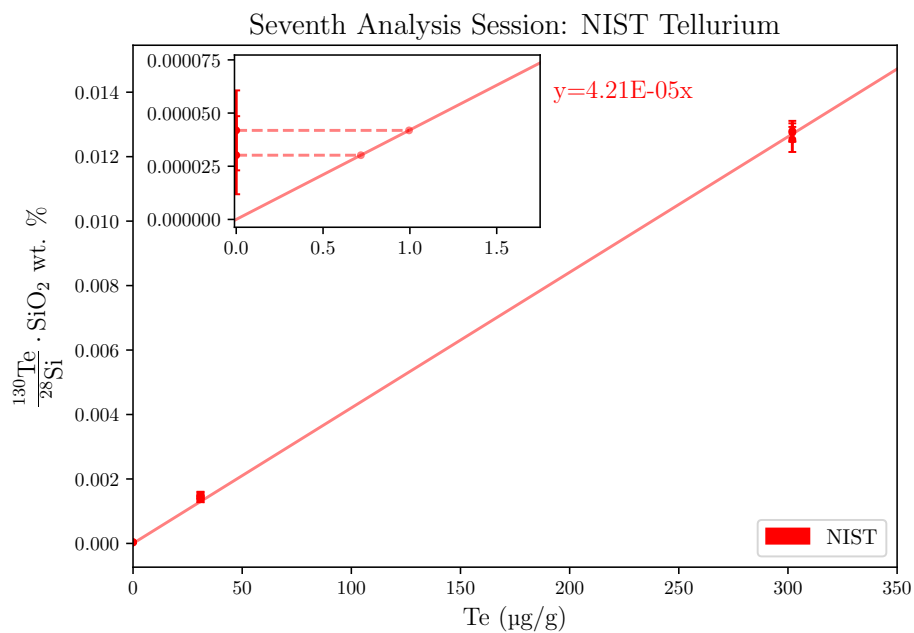
Figure 2.12: Calibration curves forced through the origin of Te in the NIST glasses from the 7th analysis session. Dashed lines in the insets show the projection of the count ratios of 614 on to the calibration curve, marking the concentration that would be calculated from the curve. The equation is of the calibration curve.
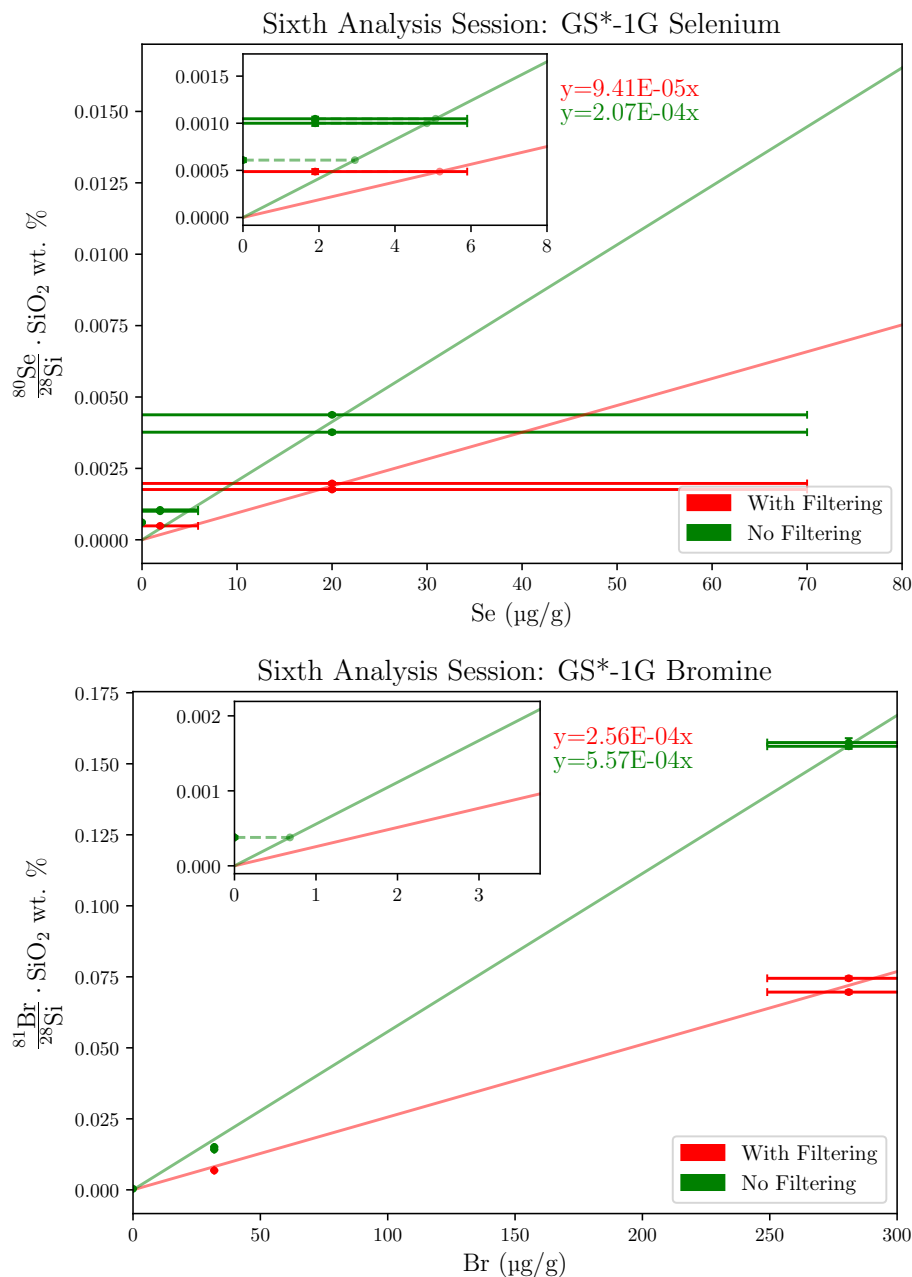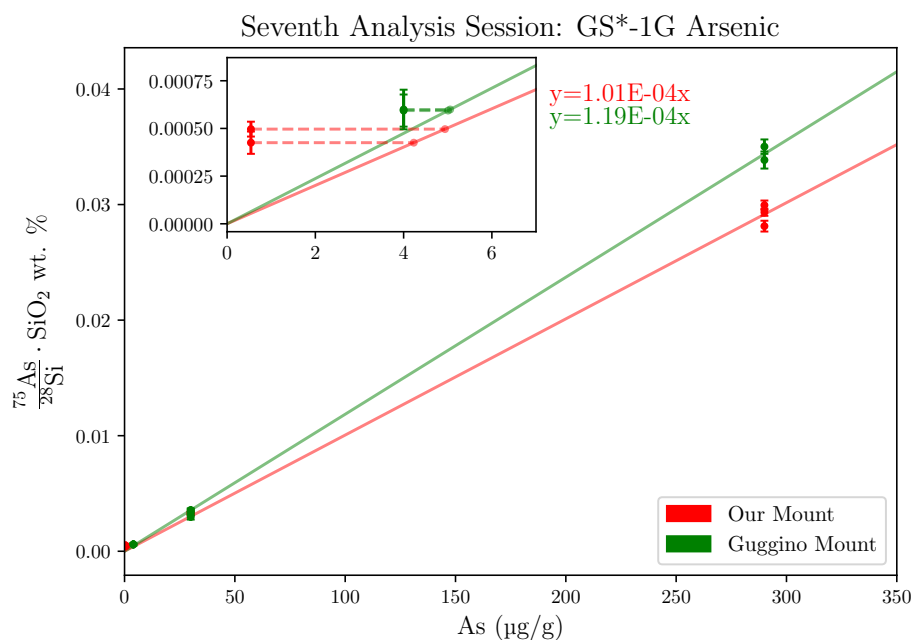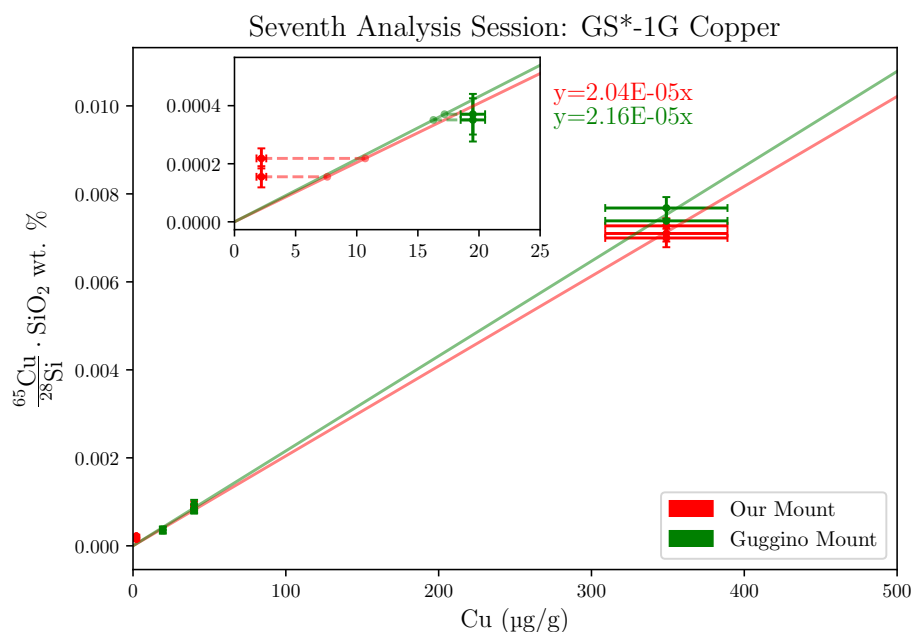
Figure 2.13: Calibration curves forced through the origin of Cu and As in the GS*-1G glasses from the 7th analysis session. The two curves were created from analyses on our mount (red) and on the "Guggino" mount (green). Dashed lines in the insets show the projection of the count ratios of GSA and GSC on to the no energy filtering curve, marking the concentration that would be calculated from the curve. The equations in red and green are of the calibration curves.

43
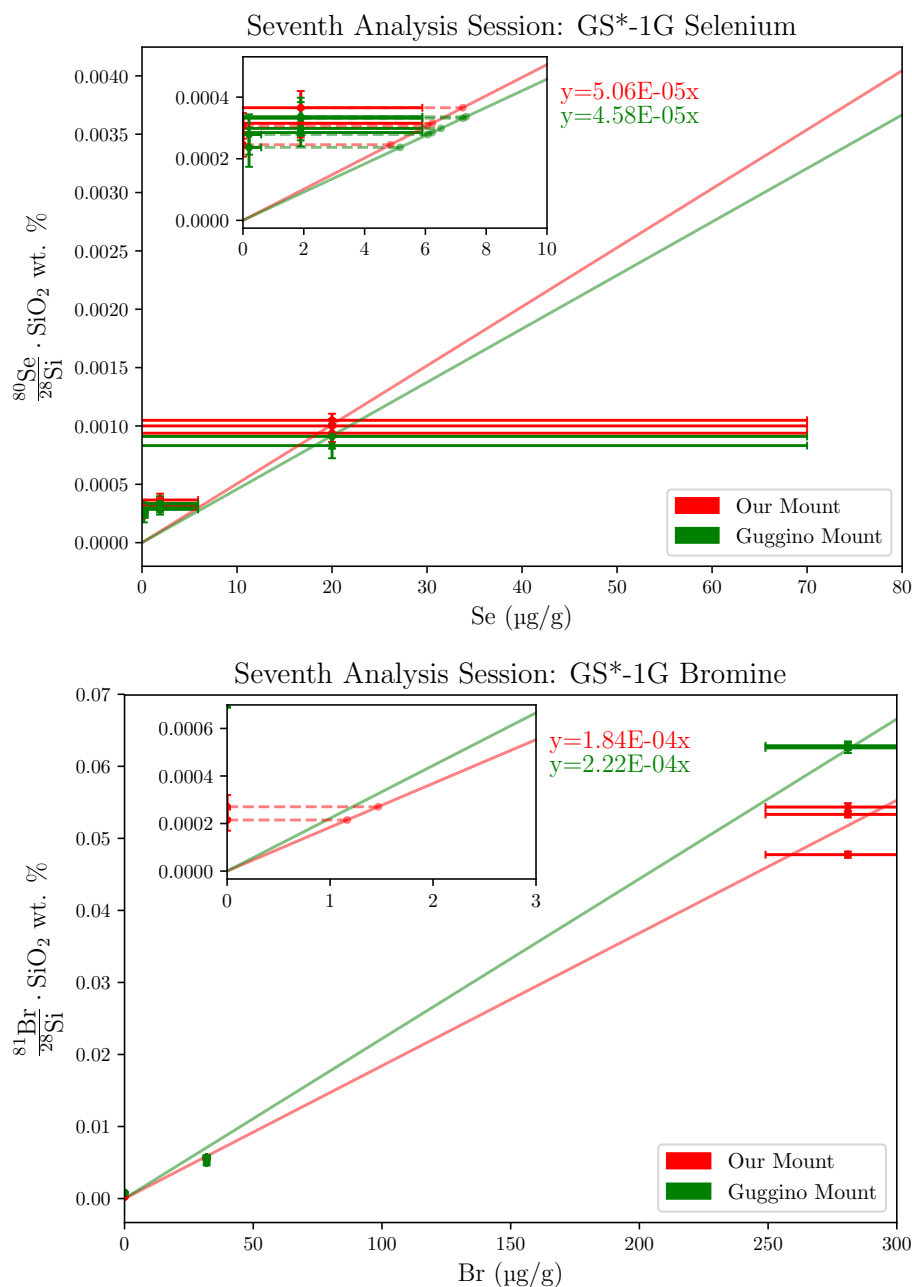
Figure 2.14: Calibration curves forced through the origin of Se and Br in the GS*-1G glasses from the 7th analysis session. The two curves were created from analyses on our mount (red) and on the "Guggino" mount (green). Dashed lines in the insets show the projection of the count ratios of GSA and GSC on to the no energy filtering curve, marking the concentration that would be calculated from the curve. The equations in red and green are of the calibration curves.
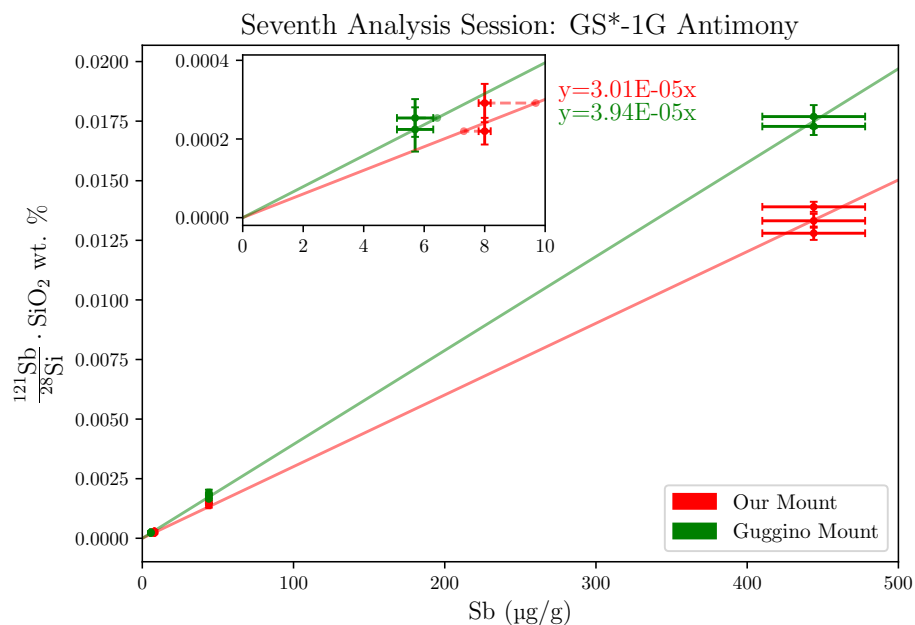
Figure 2.15: Calibration curves forced through the origin of Sb in the GS*-1G glasses from the 7th analysis session. The two curves were created from analyses on our mount (red) and on the "Guggino" mount (green). Dashed lines in the insets show the projection of the count ratios of GSA and GSC on to the no energy filtering curve, marking the concentration that would be calculated from the curve. The equations in red and green are of the calibration curves.

Chapter 3

CHALCOPHILES IN THE BANDELIER TUFF

3.1 Introduction

The Jemez Mountains volcanic field of northern New Mexico is a suite of 13-0.13 Ma basaltic to rhyolitic volcanics associated with the intersection of the Rio Grande rift with a Proterozoic cratonic suture zone along the Jemez lineament (Heiken *et al.*, 1990; Wu *et al.*, 2021). The field is dominated by the Bandelier Tuff, a unit of rhyolitic pyroclastic falls and flows erupted from two consecutive caldera forming events (Heiken *et al.*, 1990). The earlier of these two eruptions occurred 1.60 Ma, ejecting between 216 and 550 km^3 of material creating the now overprinted Toledo caldera and the Otowi Member of the Bandelier (also known as the Lower Bandelier). The Otowi consists of a basal plinian pumice (referred to as the Guaje Pumice Bed) and overlying ignimbrites (Gardner *et al.*, 2010; Heiken *et al.*, 1990).

A previous study of the Otowi by Dunbar and Hervig (1992) examining trace volatile and lithophile elements in melt inclusions found strong evidence of magma mixing from two distinct sources prior to the eruption of the ignimbrite. Most of the inclusions studied had trace element concentrations that could be explained by simple fractional crystallization of quartz and sanidine, but a small number found in the lower parts of the ignimbrite were found to be anomalous (Dunbar and Hervig, 1992). These had characteristically higher Ti and lower Cl than the rest of the inclusions, as well as higher Sr and Ba and lower Nb, Li, B, Rb, Y, Nb, and Th (Dunbar and Hervig, 1992). This suite of high Ti/Cl ratio inclusions was interpreted to represent an injection of a primitive melt shortly before the eruption of the ignimbrite (Dunbar

and Hervig, 1992).

As Dunbar and Hervig (1992) only examined the lithophiles and extremely volatile elements like F, Cl in the two suites of melt inclusions, examining how the vapor/fluid-preferring chalcophiles differ between the two might tell us more about the movement of fluids in the magma and the sources of the two magmas. Therefore, we applied the technique combining energy filtering with high MRP developed in chapter 2 to measure S, Cu, As, Se, Br, Sb, and Te in these inclusions by SIMS.

Ti vs Cl in Bandelier Melt inclusions

(a) Dunbar and Hervig (1992)

(b) Our Measurements of BB030
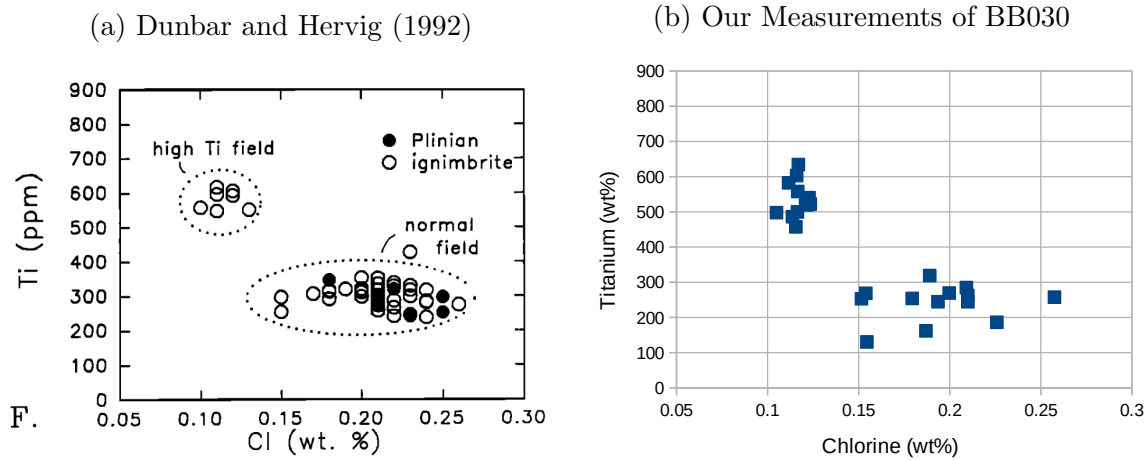
Figure 3.1: Two graphs of Ti vs Cl in the Bandelier melt inclusions. (a) The left figure was taken from Dunbar and Hervig (1992) showing their measurements. The solid points represent inclusions found in the basal plinian Guaje pumice, and hollow points represent inclusions found in the ignimbrite of the Otowi Member. Circled "normal field" represents inclusions with low Ti/Cl found throughout the Otowi, and the "High Ti field" highlights the small subset of inclusions found in the ignimbrite containing distinctly high Ti and low Cl. (b) The right figure shows our electron microprobe measurements of Ti and Cl in the inclusions from BB030, which came from a single pumice fragment from the ignimbrite. Between four and six measurements of each inclusion were made, and each individual measurement is plotted as a separate point.

3.2 Methods

3.2.1 Samples

The sample used was one of the same used in the Dunbar and Hervig (1992) paper which we obtained from Dr. Dunbar. This sample was a polished mount of quartz phenocrysts containing melt inclusions referred to as BB030 in the paper. The quartz phenocrysts were all recovered from a single pumice lump found in the Otowi ignimbrite 5m above the Guaje Pumice bed. This mount was chosen as its melt inclusions are known to belong to both high and low Ti populations allowing us to study both in a single sample. No further preparation of the sample was performed other than removing an old, damaged conductive carbon coat by Ar-ion milling and recoating the sample with carbon.

Eight melt inclusions in BB030 were selected to study. These were selected based on notes and hand drawn figures obtained from Dr. Dunbar indicating the melt inclusions had been previously examined by SIMS. These were labelled IP1, IP4, IP6, IP8, IP10, IP12, IP14, and IP15 (IP standing for ion probe, an alternative name for SIMS). Images of these inclusions are found in figures 3.2 and 3.3.

3.2.2 Measuring Major and Minor Elements

In order to properly analyze these inclusions by SIMS we need to know the weight percent SiO_2 in each inclusion to normalize our count rates to, as well as the relative proportions of Ti and Cl to identify which population each inclusion belongs to. While Dunbar and Hervig (1992) had previously made major and minor element analyses of all the inclusions in BB030, we were unable to confidently assign the values listed in the paper to individual inclusions. Therefore, an electron microprobe analysis of the

inclusions was performed measuring Si, Ti, Al, Fe, Mg, Ca, Na, K, S, and Cl in each inclusion. This was done on the JEOL JXA-8530F electron microprobe located in Arizona State University's Eyring Materials center. Analyses of the melt inclusions done on this instrument used an electron beam with a 15 kV accelerating voltage and, in order to measure Ti at trace levels, a fairly high 15 nA beam current. In order to prevent damage to the hydrous glass of the inclusions while using this high current, a large beam spot size of 20 μm was used. The results for the most important major and minor elements are presented in table 3.1. The Ti/Cl ratios obtained allowed us to confidently assign each inclusion as belonging to either the high Ti/Cl or low Ti/Cl population. IP1, 10, 14 and 15 are low Ti/Cl, having Ti/Cl ratios less than 0.25. IP4, 6, 8, and 12 are high Ti/Cl with ratios above 0.4. Additionally plotting all measurements of Ti and Cl in the inclusions produces nearly identical results to similar plots made by Dunbar and Hervig (1992) (see figure 3.1).

Major Element Composition and Ti/Cl Ratios of the Melt Inclusions

	SiO_2	Al_2O_3	FeO	CaO	Na_2O	K_2O	SO_3	Ti	Cl	Ti/Cl	Total
IP1	73.1	11.7	1.2	0.3	3.4	4.0	0.002	0.035	0.153	0.23	93.9
IP4	74.4	11.8	1.4	0.2	3.2	4.4	0.013	0.054	0.121	0.45	95.7
IP6	76.1	11.9	1.4	0.2	3.0	4.6	0.014	0.055	0.118	0.46	97.5
IP8	76.2	12.0	1.4	0.2	3.7	4.0	0.003	0.051	0.119	0.43	97.7
IP10	74.9	11.8	1.0	0.2	3.5	4.5	0.015	0.026	0.209	0.12	96.2
IP12	72.1	11.6	1.4	0.2	3.4	4.5	0.014	0.051	0.117	0.44	93.4
IP14	71.3	11.6	1.0	0.1	2.8	4.4	0.012	0.021	0.203	0.10	91.5
IP15	74.1	11.9	1.4	0.2	3.4	4.3	0.019	0.027	0.205	0.13	95.5

Table 3.1: Table of the concentrations of the major and minor elements in the BB030 melt inclusions as measured by the electron microprobe. All numbers are in units of weight percent either oxide or elemental, with the exception of the Ti/Cl ratio which is unitless. Mg was also measured, but all inclusions contained 0.0 wt.% MgO so it is not listed.

3.2.3 SIMS Procedure

All SIMS analyses were done according to the general procedure laid out in chapter 2 section 2.2.1.

3.2.4 Analyses

Three analysis sessions were performed on the melt inclusions. During these, we measured the inclusions, their surrounding quartz grains, and the NIST glasses for S, Cu, As, Se, Br, Sb, and Te. The data from the first of these sessions had to be discarded due to charging of the standard mount, drifting of the mass peaks due to hysteresis, and apparent surface contamination. The second session's results were better, but there were still issues with surface contamination and hysteresis. The third analysis session's results are preferred as we took serious precautions against previously observed issues.

Our mount containing the NIST glasses was poorly polished, and the gold coat had become damaged. Therefore, we re-polished it to a much higher standard, carefully re-applied the gold coat, and added conductive carbon paint at multiple locations at the epoxy-aluminum and epoxy-glass boundaries for each glass.

The same sample holder was used for the standard mount and BB030, rather than putting them in separate mounts so they could be loaded into the instrument at the same time. This was done as the sample holders can become deformed due to rough handling and no longer hold the sample perfectly perpendicular to the column. This causes the distance between the sample and the extraction electrode to change depending on the location being analyzed, effecting count rates. Therefore we used the most pristine sample holder available, and swapped the sample it contained between measuring the standards and BB030.

During the analyses of the melt inclusions, we avoided ever leaving the hysteresis loop of the elements being analyzed. At 3000 MRP, the mass peaks are so narrow that even tiny shifts due to hysteresis can dramatically effect counts. Normally, when moving to a new target on the sample mount one moves the magnet to a universally present and abundant ion like $^{16}O^-$ in order to locate the impact location of the beam and re-center it. We found that this was enough to upset the hysteresis of the magnet, moving the analyzed mass for Si almost to the edge of the mass peak and dramatically reducing the measured counts. Additionally, reaching steady state locations for the mass peaks again took upwards of 30 cycles afterward. Therefore, we used the last element to be analyzed in the previous analysis routine, $^{28}Si^-$, to locate the beam and any time we had to break the loop we cycled through the masses until the peaks were observed to stop shifting significantly.

During the previous analyses, we had observed that S counts often started out extremely high and dropped rapidly over the course of each analysis. We believed this to be due to some form of surface contamination, perhaps from the epoxy in the mount. In order to avoid it we specifically sampled in old sputter pits from previous analyses.

3.3 Results

The data from the third analysis session was plotted on calibration curves, using the NIST measurements taken to construct a origin-forced line which the count rates of the unknown melt inclusions were plotted on to determine their concentrations. The plots are given in figures 3.4 - 3.7, and the results in table 3.2.

Our analyses show background levels of most of the chalcophile elements and little systematic variation between the Ti-rich and Ti-poor groups. A major exception is

copper, which was measured to be around $5\,\mu g/g$ in all the low Ti/Cl inclusions, close to the previously determined molecular ion background for the similar NIST glasses. In all of the high Ti/Cl inclusions we found $30\,\mu g/g$, well above the background and any statistical fluctuations. The other exception is As. The low Ti/Cl inclusions all contain $6\,\mu g/g$ while the high Ti/Cl ones contain $4\,\mu g/g$. These are both well above the $0.3\,\mu g/g$ molecular background previously determined in the NIST glasses.

Additionally, we found two anomalous high Ti/Cl inclusions, IP6 and IP12. These two both displayed initially extremely high S counts that declined rapidly over time, what we believed to represent surface contamination, despite being in previous sputter pits. In these cases, not only did the sulfur count rates start high but Br, Sb, and Te did as well, similarly declining over the course of the analysis. We performed a second analysis of IP6 immediately after the first in the same location. All count rates had reached steady state during this analysis. The Sb and Te levels were lower but still significantly elevated, giving 24 ppm Sb and 5 ppm Te respectively.

3.4   Discussion

Despite working with an extremely small sample set and having previously shown that the technique we used combining high MRP and energy filtering only reduces precision and count rates, we were still able to identify some interesting patterns in the chalcophile concentrations of the melt inclusions. We found a substantial and extremely consistent difference in the Cu concentrations of the inclusions from the primitive high Ti/Cl magma compared to the evolved low Ti/Cl magma. One might conjecture that this difference is simply due to the evolved body having lost most of its Cu to a fluid/vapor phase as it evolved. However, if we assume that the two magmas originally had similar Cu concentrations (meaning that the evolved magma lost $25\,\mu g/g$), that the high Ti/Cl material makes up an insignifcant portion of the

Chalcophile Concentrations in BB030 Melt Inclusions

	Inclusion	Ti/Cl	S	Cu	As	Se	Sb	Te
Low Ti/Cl	IP1	0.23	30.85	9.63	6.25	1.10	2.51	0.70
	IP10	0.12	14.3	3.9	6.6	1.1	2.5	0.9
	IP14	0.10	19.8	5.6	6.0	0.9	4.1	1.8
	IP15	0.13	20.7	5.1	5.9	0.6	4.4	1.0
High Ti/Cl	IP4	0.45	36.7	32.1	2.8	0.4	1.9	0.5
	IP6-1	0.46	230.3	29.9	3.4	1.4	60.4	20.5
	IP6-2	0.46	73.5	27.4	3.2	0.6	23.7	5.2
	IP8	0.43	36.9	39.1	3.4	0.5	2.2	0.6
	IP12	0.44	236.6	37.1	4.3	0.9	23.4	4.0
Quartz	Qtz 1	-	0.8	2.3	0.4	0.1	1.5	0.7
	Qtz 2	-	2.5	3.0	0.4	0.2	1.2	0.6

Table 3.2: Chalcophile concentrations of the melt inclusions as measured during the third analysis session. All numbers are in units of µg/g. The two consecutive measurements of IP6 are listed separately, with the first showing dramatically higher S, Sb, and Te concentrations due to the initially high then rapidly dropping count rates of these elements. Additionally, two measurements of the quartz phenocrysts surrounding IP1 and IP6 are presented.

erupted material (reasonable since we see very few low Ti/Cl inclusions), a rhyolite density of 2700 kg/m^3, and that the volume of erupted dense-rock equivalent is in the middle of the estimated range at 300km^3, that means the erupted material alone would have lost a staggering 2×10^7 metric tons of Cu, which is about the same as the estimated reserves of the largest copper mine in the world, Escondida (Padilla-Garza, 2001). Clearly this is not reasonable. Thus a better explanation would be that either the primitive magma came from a very different source material or it assimilated some very Cu-rich wall rock before entering the chamber. Studies of zircons in the Bandelier have shown the magma that formed the Otowi came from at least three separate plutons/basement rock sources (Wu *et al.*, 2021). Additionally, there are known

copper mineralized strata of Triassic age in this area (Lucas and Heckert, 1996). The evolved melt contains more arsenic than the primitive injected liquid. This is also evidence for a different source of the high-Ti melt as this is the opposite of what one would expect if the difference were simply due to loss of As to a fluid/vapor phase.

In addition to systematic differences in Cu and As, we also observed two anomalous high Ti/Cl inclusions IP6 and IP12. These inclusions showed initially extremely high count rates of S, Br, Sb, and Te that dropped rapidly over the course of the initial analyses. This at first glance would suggest that the surface of the sample was contaminated. However not only were we sampling in our previous SIMS pits, so any contamination would have had to been introduced between the second and third sessions, but we also sampled the quartz grain containing IP6 near the inclusion (labelled Qtz 2 in table 3.2) and observed only background levels of these elements. Compounding this is the fact that Br, Sb, and Te are rare to extremely rare elements in the crust and to our knowledge is not found in any man-made contaminant that our sample could have been exposed to. Another possible explanation lies in the nature of the inclusions themselves. Both IP6 and 12 are visually distinctive, containing a significant amount of vapor bubbles (see figure 3.3). Due to the size of IP6 and the even distribution of tiny bubbles in IP12, we were forced to put the primary beam partially on these bubbles. It is conceivable that a salt rich in S, Br, Sb, and Te precipitated from the fluid/vapor contained in these bubbles. The fact that the count rates of Br, Sb, and Te are all linearly correlated with S suggests that there was only one salt phase containing all these elements. If this is true, then our drop in count rates would then simply represent initially sputtering into a vapor bubble and then through a grain or thin layer of this salt. However, all the S, Br, Sb, and Te measured in these two inclusions did not come from this salt. The second analysis of IP6 reached a steady state in the counts of these elements which would imply the

S-rich phase, salt or contaminant, had been sputtered through completely. Still, the concentrations of these elements in this analysis were well above all the other inclusions. Thus this inclusion is still rich in these elements regardless of the source of the S-rich phase. This analysis of the glass alone shows $\sim$23 µg/g and $\sim$4 µg/g of Sb and Te respectively subtracting for the approximately 0.5 µg/g and 1 µg/g backgrounds determined previously for NIST. These concentrations are far above crustal averages, with Sb having an estimated concentration in the crust of 0.2 µg/g and Te having an estimated concentration of a mere 0.005 µg/g (Wedepohl, 1995). Unfortunately, we cannot say how enriched in Br the inclusion is as the NIST glasses contain too little of the element to make a usable calibration curve.

The fact that IP6 and 12 are the only two primitive melt inclusions to show such extreme enrichments of Sb and Te, as well as higher Br count rates, requires explanation. As IP6 and 12 contain a significant portion of their volume as vapor bubbles, we might speculate that the primitive high Ti/Cl magma was initially enriched in these elements, and lost them early on to outgassing of a vapor after mingling with the volatile-saturated main magma. Melt inclusions trapped early on might still contain these elements (along with exsolving vapor) while those trapped later would not contain significant amounts of the elements. There is a slight negative correlation between Ti/Cl and As, Sb, and Te in the inclusions, excluding IP6 and 12, which might support this. However, we see no such correlation for S and Cu, and in fact S has a slight positive correlation with the Ti/Cl ratios. This raises the question of why, if such a fluid/vapor existed, only some of the chalcophiles strongly partitioned into it while others were barely (if at all) affected despite the volatility of the elements.

3.5 Conclusion

By examining S, Cu, As, Se, Br, Sb, and Te in melt inclusions from the Otowi Member of the Bandelier Tuff we were able to identify a few interesting variations in the concentrations of these elements at µg/g levels between the previously identified primitive and evolved melts that suggest they may have come from different source materials. Additionally, two primitive melt inclusions were found to be strongly enriched in S, Br, Sb, and Te suggesting the possible existence of a vapor phase which could have scavenged select chalophiles from the primitive melt shortly after being injected into the chamber. Given our extremely small sample size, it is hard to say anything definitive other than that these elements can tell us more about the histories of the magmas. A more thorough investigation of a much larger number of melt inclusions from the Otowi and perhaps the inter-caldera Cerro Toledo Formation erupted after the Otowi would make the subtle variations we observed more obvious and any conclusions drawn more concrete.

Reflected and BSE Images of Melt Inclusions 1

(a) IP1

(b) IP4

(c) IP8

(d) IP10

(e) IP14

(f) IP15
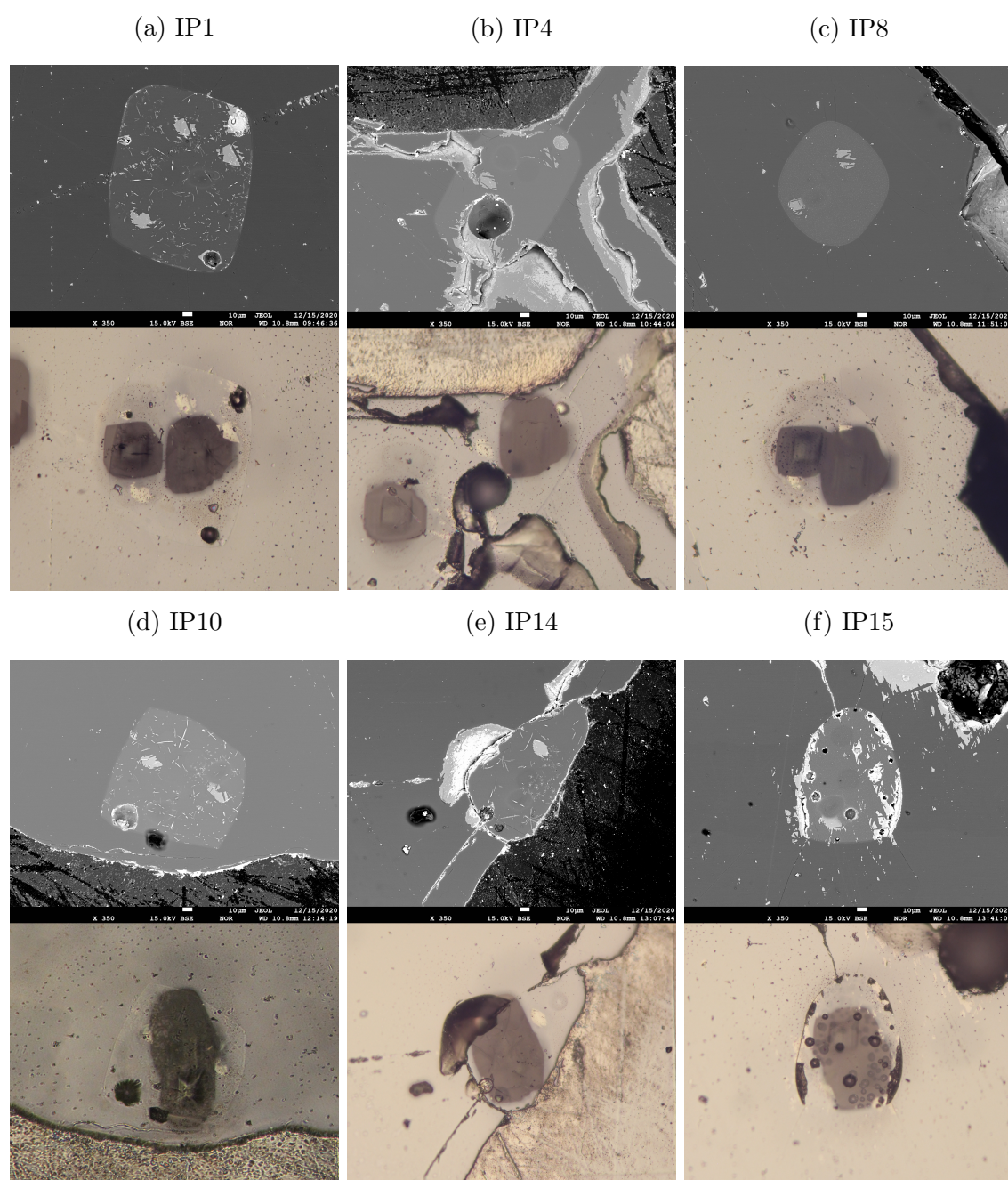
Figure 3.2: Reflected light and back-scattered electron (BSE) images of the inclusions IP1, 4, 8, 10, 14, and 15. Bright, patchy areas in the BSE images are remnants of a poorly removed gold coat.

Reflected and BSE Images of Melt Inclusions 2

(a) IP6　　　　　　　　　　　　　　　　(b) IP12
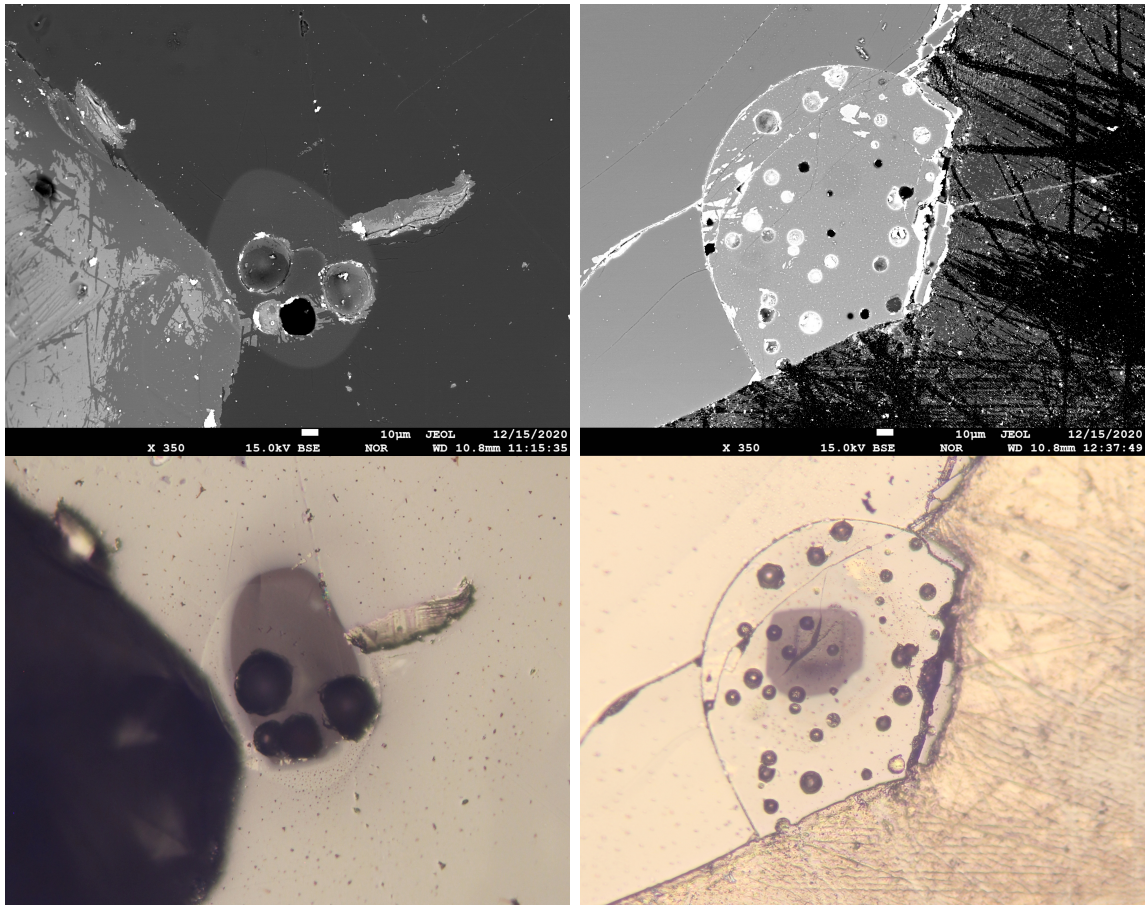
Figure 3.3: Reflected light and back-scattered electron (BSE) images of the inclusions IP6 and 12

Figure 3.4: Concentrations of S and Cu in the melt inclusions as determined from NIST calibration curves from the third analysis session. Red points are the NIST standards, green points are the low Ti/Cl inclusions (IP1, 10, 14, and 15), blue points are the high Ti/Cl (IP4, 6, 8 and 12), and cyan are measurements of the quartz phenocrysts.
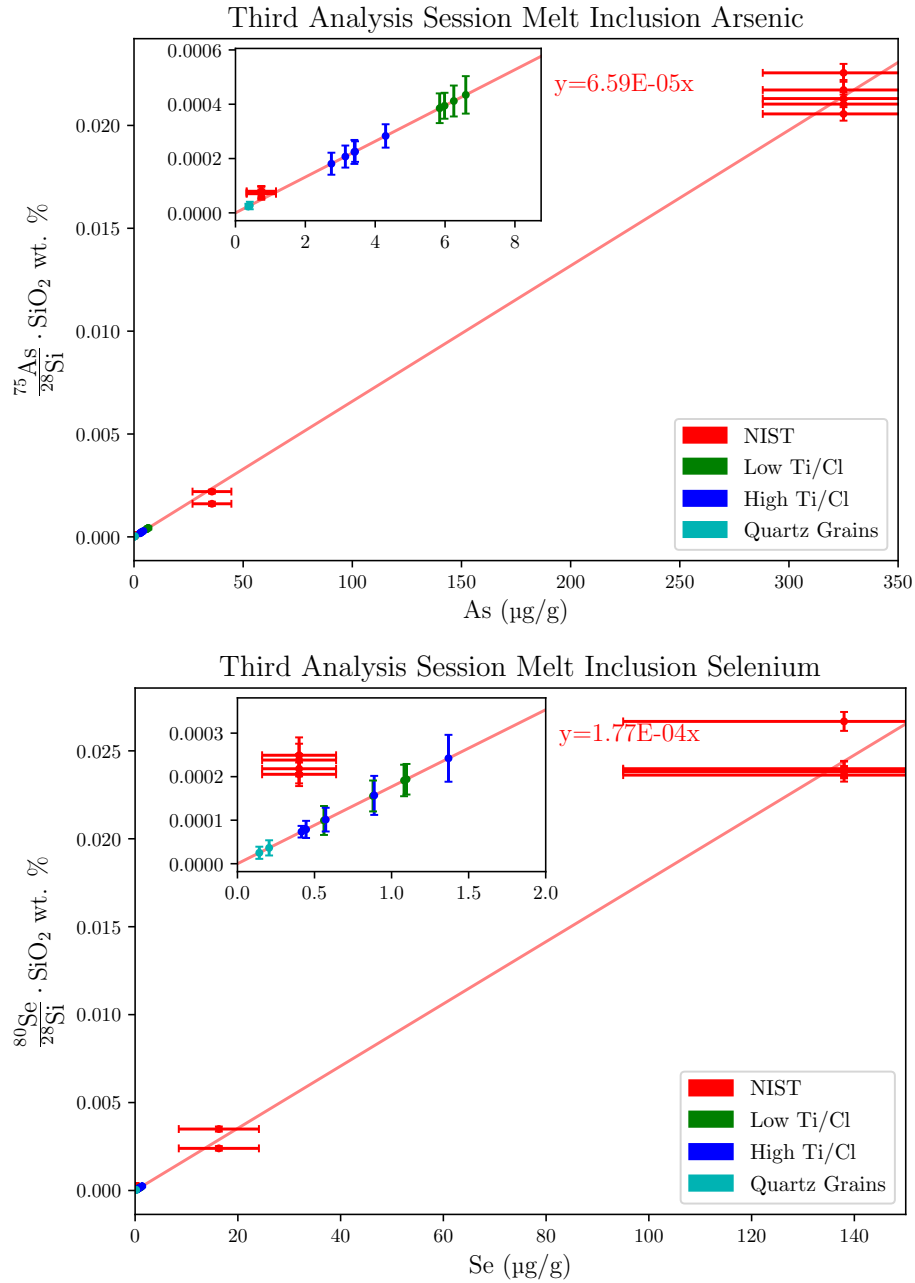
Figure 3.5: Concentrations of As and Se in the melt inclusions as determined from NIST calibration curves from the third analysis session. Red points are the NIST standards, green points are the low Ti/Cl inclusions (IP1, 10, 14, and 15), blue points are the high Ti/Cl (IP4, 6, 8 and 12), and cyan are measurements of the quartz phenocrysts
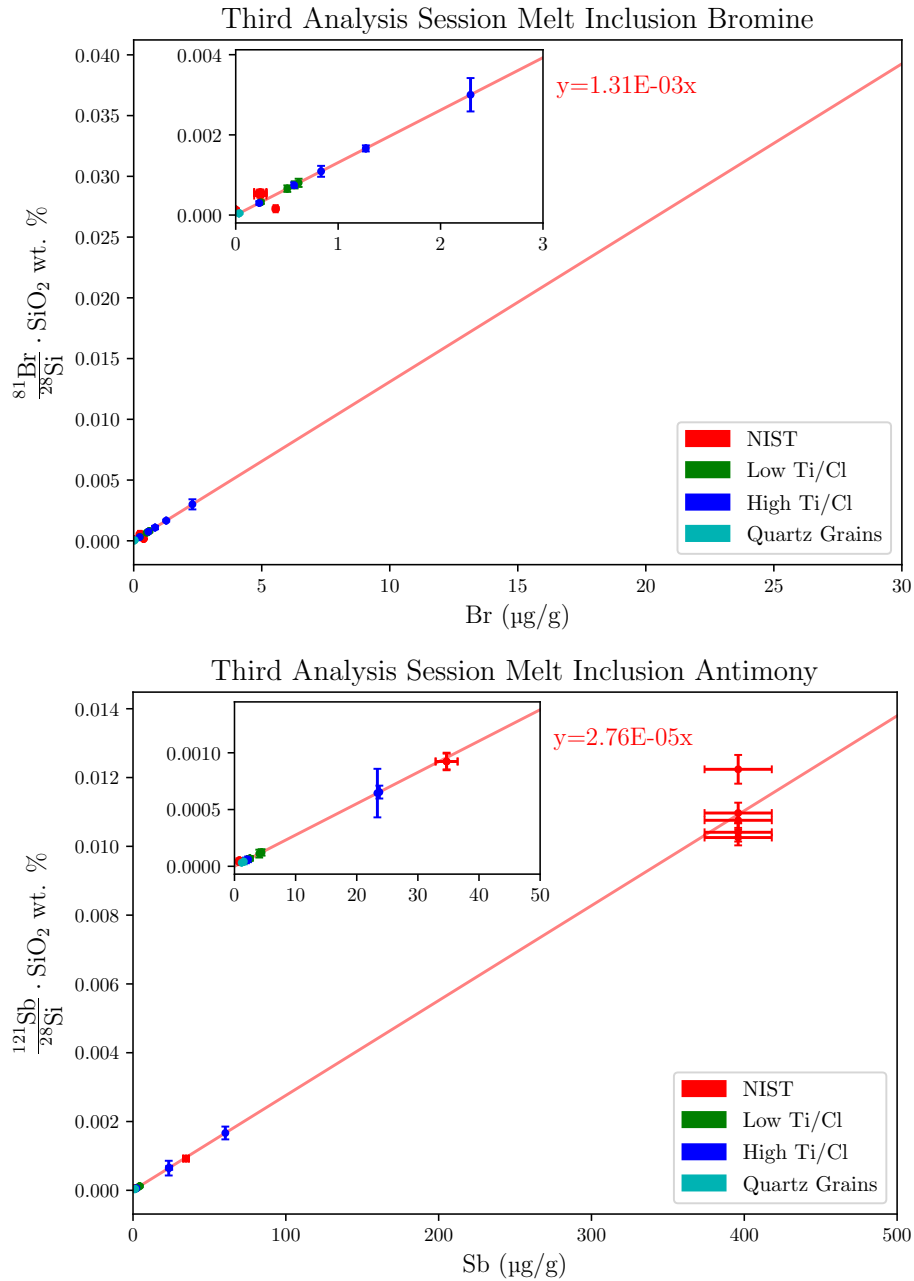
Figure 3.6: Concentrations of Br and Sb in the melt inclusions as determined from NIST calibration curves from the third analysis session. Red points are the NIST standards, green points are the low Ti/Cl inclusions (IP1, 10, 14, and 15), blue points are the high Ti/Cl (IP4, 6, 8 and 12), and cyan are measurements of the quartz phenocrysts

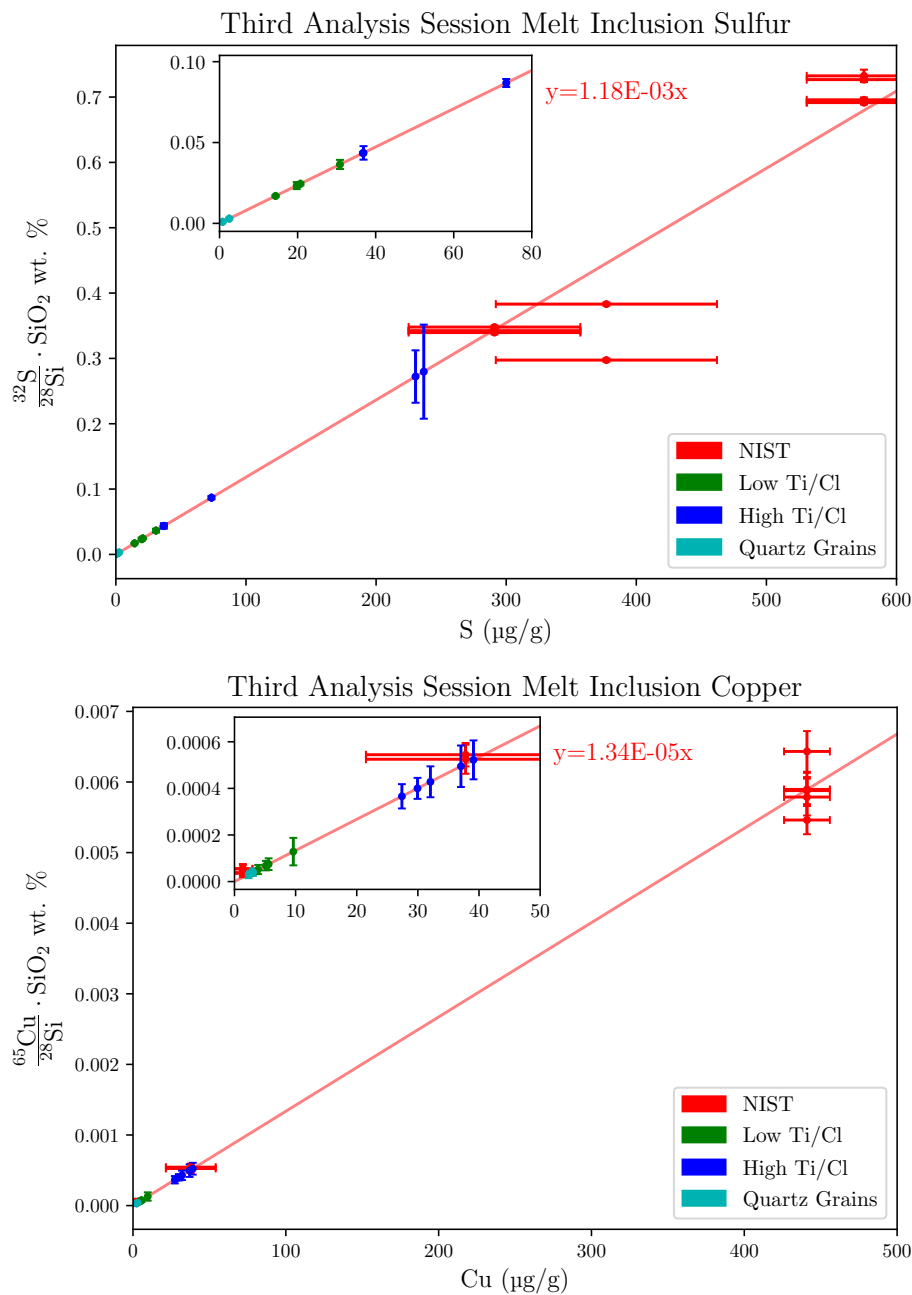Figure 3.7: Concentrations of Te in the melt inclusions as determined from NIST calibration curves from the third analysis session. Red points are the NIST standards, green points are the low Ti/Cl inclusions (IP1, 10, 14, and 15), blue points are the high Ti/Cl (IP4, 6, 8 and 12), and cyan are measurements of the quartz phenocrysts
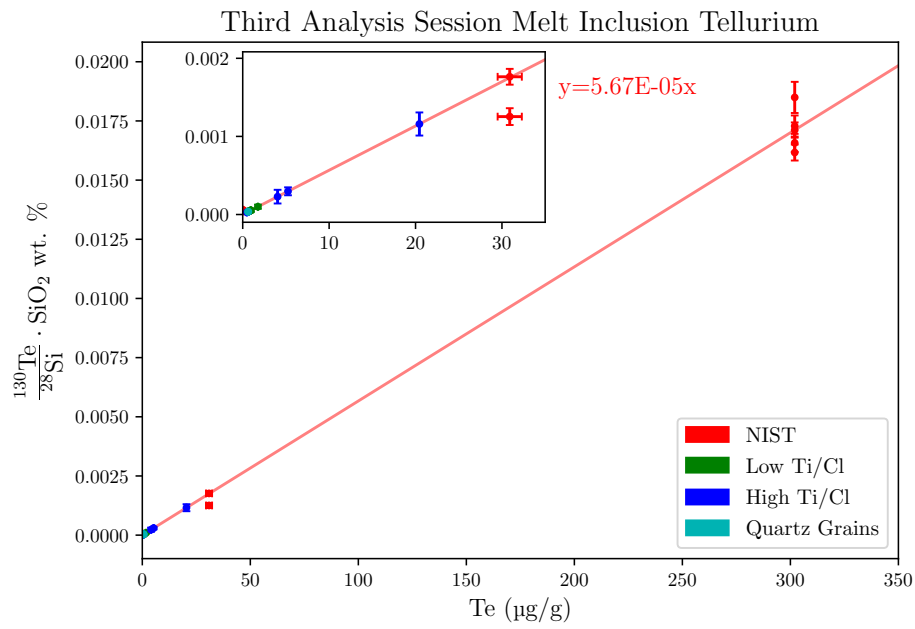
Chapter 4

SECONDARY ION MASS SPECTROMETER ANALYSES FOR TRACE
ELEMENTS USING SINGLY AND DOUBLY CHARGED SILICON IONS FOR
NORMALIZATION

4.1   Introduction

SIMS is particularly sensitive to many elements, but the three light lithophile
elements, lithium, beryllium, and boron have represented a particular focus for this
technique. There are many examples of the calibration of SIMS for these elements
(e.g., Hervig (2002); Ottolini *et al.* (1993)), and several examples show that major
element chemistry variations do not play a large role in changing the calibration factor
(e.g., Ottolini *et al.* (1993); Dunham *et al.* (2020)). That is, the effect of chemistry
on the ion yield of these elements tends to be small. Many SIMS calibrations involve
normalizing the intensity of the ion of interest to a matrix ion, such as one of the silicon
isotopes when studying silicate minerals and glasses. The normalization is important
because (at least in the Cameca ims design) there is a very strong potential gradient
between the sample and the grounded extraction lens, and if the distance between
the sample and ground changes (resulting from tilted samples or sample holders), the
absolute count rates can change, while ion ratios (e.g., Li^+/Si^+) will vary less as the
sample is moved to examine different areas.

Some earlier published results consciously selected secondary ions ejected with
several tens of eV initial kinetic energy (the energy filtering approach; e.g., Shimizu
and Hart (1982)) while other researchers have used low-energy secondary ions (most
abundant; e.g., Dunham *et al.* (2020)). These results are consistent in that the

normalizing ion was most often singly-charged silicon. However, silicon (like many other elements) will form abundant multiply charged ions (such as Si^{2+}, Si^{3+}, and even Si^{4+}), for which the signal shows up at mass/charge of 14, 9.3, and 7, assuming the most abundant isotope, ^{28}Si, is detected. The attraction of using, for example, the doubly charged ion is that the count rate is several hundred times smaller than the elemental ion, allowing the operator to increase the primary beam current to remove more trace element atoms and increase sensitivity while not increasing analysis time. In addition, when using large-geometry SIMS instruments to study concentrations or isotope ratios of light elements (Li to B) collecting a signal for silicon using Si^{3+} or Si^{2+} requires a smaller change in the magnetic field (see, for example, Dunham *et al.* (2020)).

There is nothing intrinsically wrong with using multiply-charged ions in SIMS. For example, Riciputi *et al.* (1993) asserted that calibrations for rare earth elements using doubly-charged ions were robust. Ottolini (2002) used Ca^{2+}/Si^{2+} ion ratios to quantify the Ca content of olivine, and Harrison *et al.* (2010) used doubly charged ions to aid in determining ages of feldspars using the ^{40}K-^{40}Ca system. Doubly charged ions have been used to help understand the sputtering process itself (e.g., Schauer and Williams (1992); Franzreb *et al.* (2004)).

However, one must be aware that doubly-charged ions cannot be substituted for singly-charged species without careful consideration. For example, if one places a potential of 10,000V on the sample, singly-charged ions are accelerated to 10 keV energies (plus any initial energy resulting from the collision cascade). Doubly-charged ions will be accelerated to 20 keV energies! As a result, when using an electron multiplier detector, the efficiency of pulse detection may be greater when the higher energy ion strikes the first dynode, and aging of the electron multiplier (even during a single analysis session) may result in measurable decreases in M^+/Si^{2+} ratios from

a constant matrix over time. Such observations stopped the ASU lab from using Si^{2+} in the early 1990s, as session to session reproducibility on standards decreased significantly (ASU lab, unpublished data). Another consideration is whether the process that generates multiply-charged ions is similar to that which generates singly-charged ions. Schauer and Williams (1992) showed that not only are the energy spectra of 1+ and 2+ ions from pure metals different, their response to oxygen flooding is different. The latter observation may indicate that the yield of 2+ ions may depend on the oxygen content of the sputtered crater floor. This parameter will change with sputter yield (atoms ejected per incoming primary ion), and may not track with the yields of 1+ ions. In this chapter, we have tested the effect of normalizing Li^+ , Be^+ and B^+ sputtered from US Geological Survey basaltic glass standards and NIST 610-614 high-silica glasses (Jochum *et al.*, 2005, 2011) to either Si^+ or Si^{2+} and describe changes in the resulting calibration curves as a function of matrix chemistry.

4.2   Analytical Methods

We used the Cameca ims 6f SIMS at ASU for this work. The samples above were sputtered using a mass-filtered beam of $^{16}O^-$ formed in a modified Cameca duo-plasmatron at a current of $\sim$3nA and rastered over a 10×10 µm^2 area. Positive secondary ions were accelerated to 5000V, with a combination of transfer optics and field apertures used to sample a 15 µm diameter circular area including most of the sputtered crater. The energy window was set to allow ions with a $\sim$40 eV range in energy into the mass spectrometer, and two sets of data were obtained: secondary ions with $\sim 0 \pm 20$ eV and ions with -75 ± 20 eV. All secondary ions were detected using an electron multiplier in pulse counting mode. The mass resolving power was $\sim$500 at these conditions. Counting times on the trace elements were sufficient to reach better than 10% statistical precision.

4.3 Results

Primary ion impacts result in sputtered ions with a range of initial kinetic energy, and the energy spectra of $^{30}Si^+$ and $^{28}Si^{2+}$ is shown in Figure 4.1. Note this spectra shows data from a session where the sample potential was at 9000 V. When the secondary ion count rates are examined on a log scale (right axis), the two spectra have very similar shapes. However, when the ratio of the two signals is shown on a linear scale, there appears to be significant differences between the energy spectra of the two silicon species. Thus dividing any trace ion signal by the doubly charged silicon ion might be expected to show different relations than normalizing to singly charged silicon. As shown in Figure 2, calibration curves for Li, Be, and B are very similar whether the Geological Survey basaltic glasses or the high-silica NIST 610 glass are considered. This suggests that a basaltic glass can be used to obtain accurate analyses for light lithophile elements in higher-silica glasses simply by normalizing the M+/Si+ ion ratio by the silica abundance (in wt. %). The worst-case is for Li (a $\sim$20% difference in calibration slopes) while Be and B calibrations are within $\sim$ 5%. In contrast, examination of Figure 3 shows different behavior. In this set of calibration curves (obtained in the same analyses as those in Figure 2), the NIST glass is distinctly different than the basaltic glasses. Here, the difference in calibration factor (as indicated by the slopes of lines fit through the origin) between the basaltic glasses and the NIST 610 sample is a factor of $\sim$1.5, for all elements! Because Schauer and Williams (1992) observed a difference in the energy spectra of doubly-charged ions versus singly-charged ions, we also collected ion intensities of high-energy (75 ± 20 eV initial kinetic energy) to compare calibrations of M^+/Si^+ with M^+/Si^{2+} using conventional energy filtering. As shown in Figure 4.4, matrix effects between basaltic and

high-silica glasses when normalizing to singly-charged silicon show approximately the same magnitude as when low-energy secondary ions are used (Fig. 4.2), with a maximum dispersion in the calibration slopes <30%. When secondary ions with 75 ± 20 eV initial kinetic energy are normalized to doubly-charged silicon (Figure 4.5), the effect of matrix is more pronounced than in Figure 4.4, with beryllium and boron calibrations changing by a factor of 1.5 between basaltic glass and the high-silica NIST composition. While the results shown here are from one analysis session, we have observed this enhancement of matrix effects whenever we have attempted to use doubly-charged silicon. For example, we also conducted an analysis session (only shown in Figure 4.1) where the sample potential was increased from 5000 to 9000V. Lithium showed very similar behavior as noted in Figures 4.2-4.5, but we also examined Rb, Sr, Y, Zr, Ba, Ce, Pb, Th, and U (using 75 eV ions to minimize molecular ion contribution to the mass spectrum). All elements studied showed a much larger matrix effect between the USGS basaltic glasses and the high-silica NIST glasses when doubly charged silicon was the normalizing ion compared to singly charged silicon.

4.4   Conclusion

In conclusion, using Si^{2+} as a normalizing ion species will lead to significant matrix effects in SIMS analysis, avoidable only by using standards similar in chemistry to unknowns. There are examples where doubly-charged silicon will not negatively influence the SIMS analyses. Any time the matrix is unchanging, such as step scans across crystals zoned only in trace elements, or in depth profiling analyses, it would be quite appropriate to select $^{28}Si^{2+}$. In fact, we have used this species as a check on charging during depth profiles of insulators, and obtained the same overall results (diffusion coefficients) as profiles where $^{30}Si^+$ was used for monitoring charging in sputtered craters. Because some SIMS labs have used Si^{3+} for normalizing purposes,

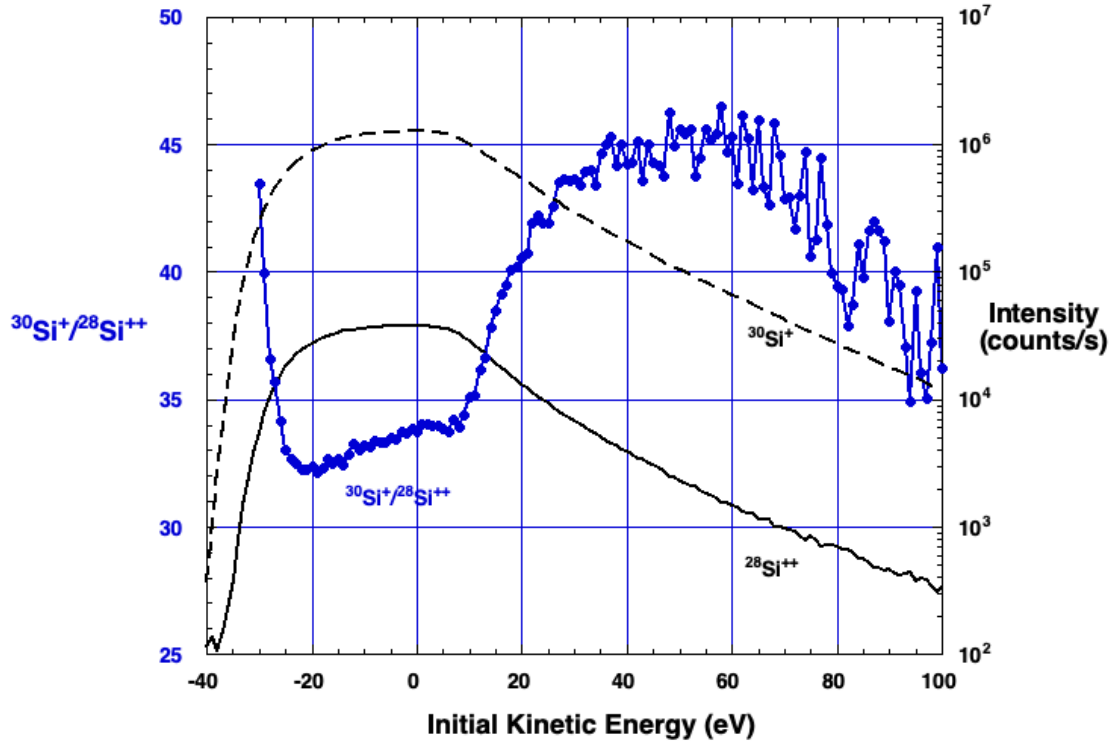we suggest this would be a good item for further study.

Figure 4.1: Energy spectra for singly and doubly charged silicon ions sputtered from one of the NIST high-silica glasses. The absolute count rates are shown on the right axis, and the ratio of the two signals are represented (in blue) on the left vertical axis. In fact, the Si_{2+} ions have 2x the energy indicated, but the x-axis is not corrected and show the signal intensities (and ratios) at the energy a trace positive ion would be normalized. This data was taken during a session where the sample potential was 9 kV.

Figure 4.2: Calibration curves for Li, Be, and B, using low energy ions (with a 40 eV energy window) normalized to the count rate for $^{30}Si^+$ and the SiO_2 content of the glass, either basaltic or in NIST 610 (70%). Note that the linear fits to the data are forced through the origin.

Figure 4.3: Calibration curves for Li, Be, and B, using low energy ions (with a 40 eV energy window) normalized to the count rate for $^{28}Si^{2+}$ and the SiO_2 content of the glass, either basaltic or in NIST 610 (70%).
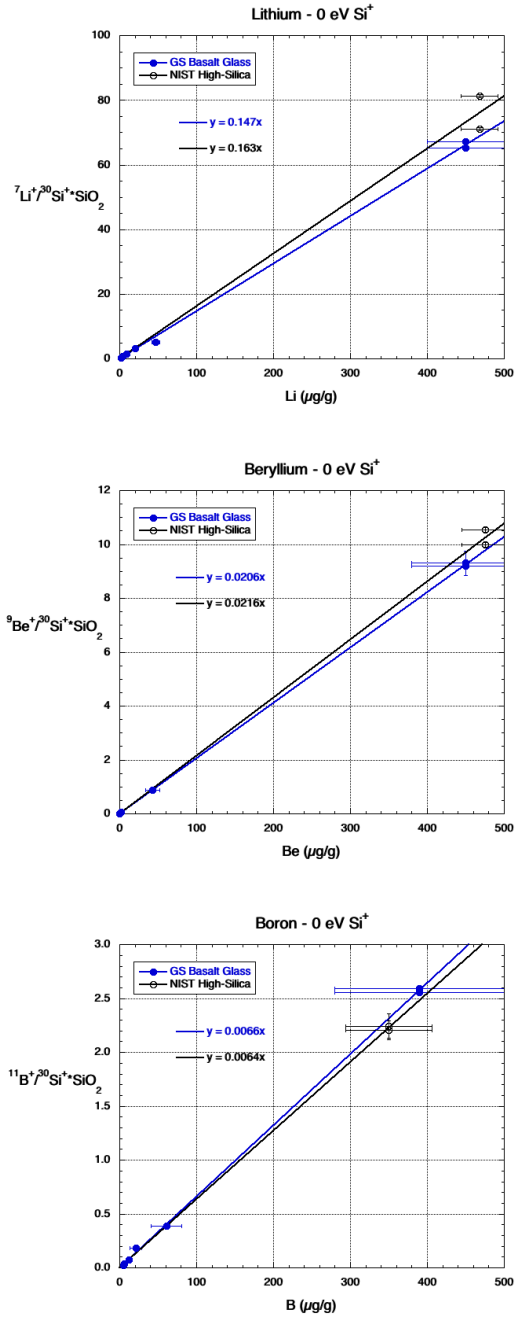
Figure 4.4: Calibration curves for Li, Be, and B, using 75 ± 20 energy ions (with a 40 eV energy window) normalized to the count rate for $^{30}Si^+$ and the SiO_2 content of the glass, either basaltic or in NIST 610 (70%).
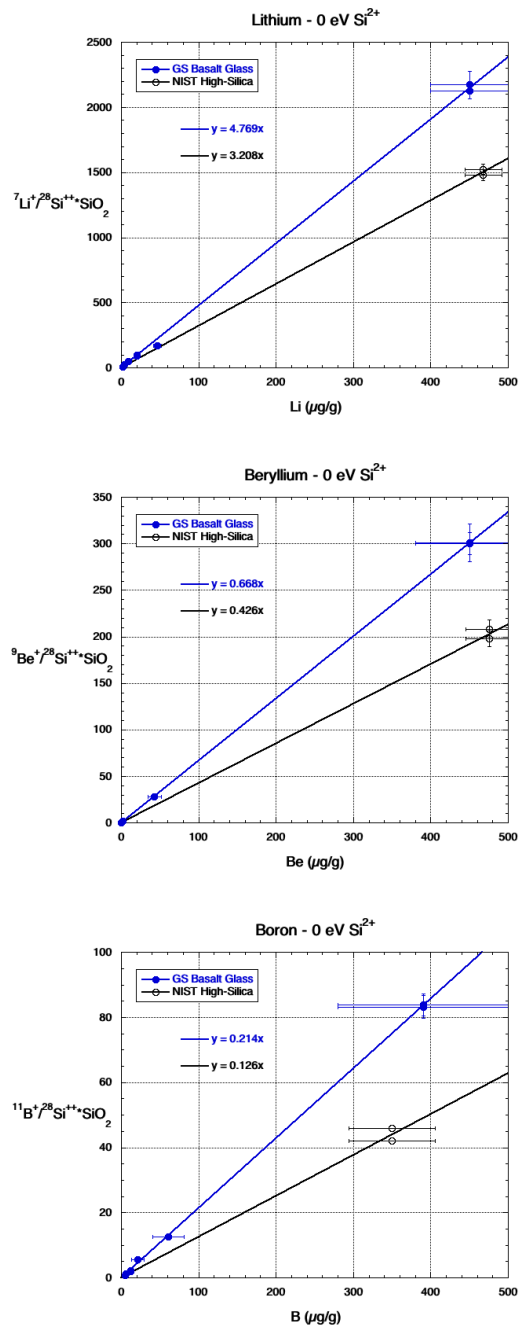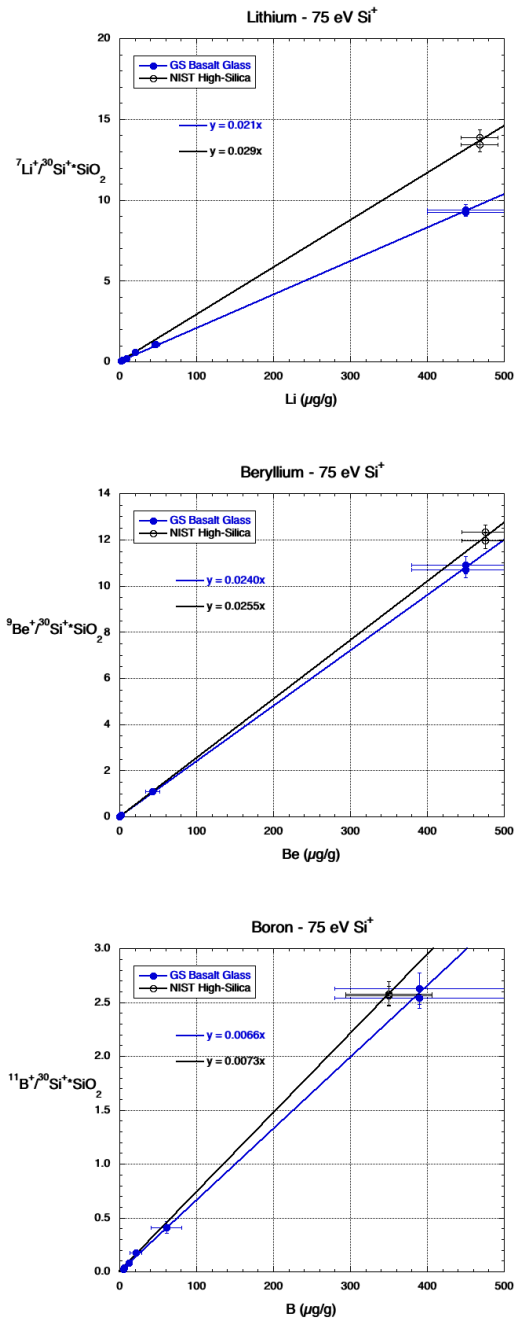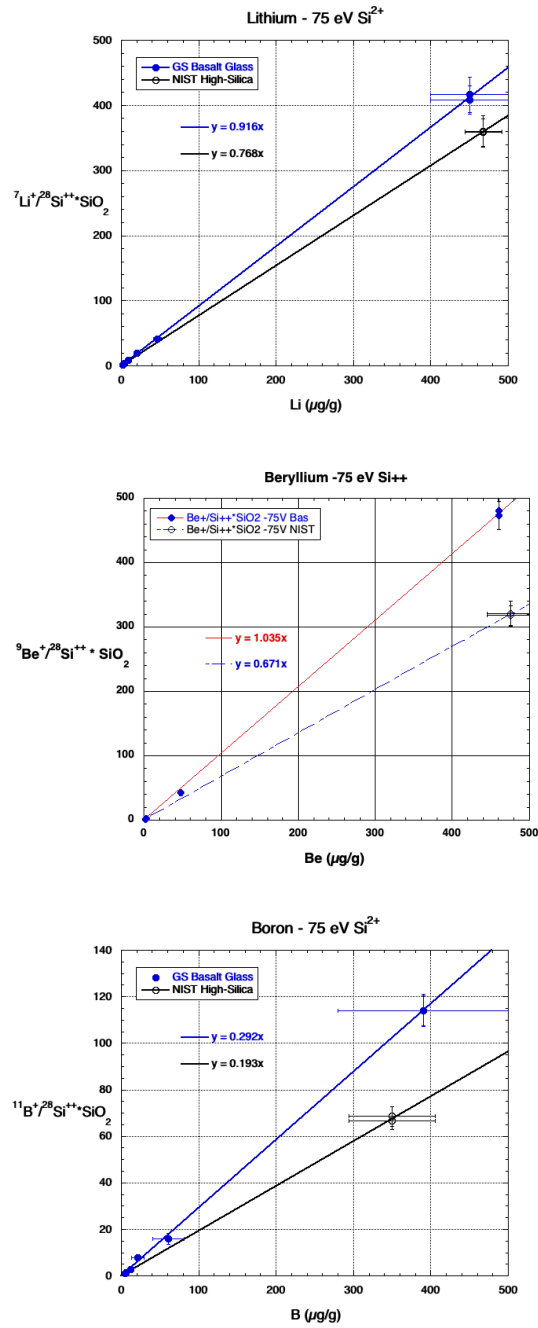
Figure 4.5: Calibration curves for Li, Be, and B, using 75 ± 20 energy ions (with a 40 eV energy window) normalized to the count rate for $^{28}Si^{2+}$ and the SiO_2 content of the glass, either basaltic or in NIST 610 (70%).

REFERENCES

Anders, E. and N. Grevesse, "Abundances of the elements: Meteoritic and solar", Geochimica et Cosmochimica acta **53**, 1, 197–214 (1989).

Barnes, S.-J., *Chalcophile Elements*, pp. 1–5 (Springer International Publishing, Cham, 2017).

Barnes, S.-J. and E. M. Ripley, "Highly siderophile and strongly chalcophile elements in magmatic ore deposits", Reviews in Mineralogy and Geochemistry **81**, 1, 725–774 (2016).

Chen, J., S. Schauer and R. Hervig, "Normal-incidence electron gun alignment method for negative ion analysis on insulators by magnetic sector SIMS", Nuclear Instruments and Methods in Physics Research Section B: Beam Interactions with Materials and Atoms **295**, 50–54 (2013).

Crozaz, G. and E. Zinner, "Ion probe determinations of the rare earth concentrations of individual meteoritic phosphate grains", Earth and Planetary Science Letters **73**, 1, 41–52 (1985).

Dunbar, N. W. and R. L. Hervig, "Volatile and trace element composition of melt inclusions from the Lower Bandelier Tuff: implications for magma chamber processes and eruptive style", Journal of Geophysical Research: Solid Earth **97**, B11, 15151–15170 (1992).

Dunham, E. T., M. Wadhwa, S. J. Desch and R. L. Hervig, "Best practices for determination of initial ^{10}Be/^{9}Be in early solar system materials by secondary ion mass spectrometry", Geostandards and geoanalytical research **44**, 4, 695–710 (2020).

Franzreb, K., R. C. Sobers, J. Lörinčík and P. Williams, "Formation of doubly positively charged diatomic ions of Mo_2^{2+} produced by Ar^+ sputtering of an Mo metal surface", The Journal of Chemical Physics **120**, 17, 7983–7986, URL `https://doi.org/10.1063/1.1690234` (2004).

Gardner, J. N., F. Goff, S. Kelley and E. Jacobs, "Rhyolites and associated deposits of the Valles-Toledo caldera complex", New Mexico Geology **32**, 1, 3–18 (2010).

Guillong, M., K. Hametner, E. Reusser, S. A. Wilson and D. Günther, "Preliminary characterisation of new glass reference materials (GSA-1G, GSC-1G, GSD-1G and GSE-1G) by laser ablation-inductively coupled plasma-mass spectrometry using 193 nm, 213 nm and 266 nm wavelengths", Geostandards and Geoanalytical Research **29**, 3, 315–331 (2005).

Harrison, T. M., M. T. Heizler, K. D. McKeegan and A. K. Schmitt, "In situ ^{40}K–^{40}Ca 'double-plus' SIMS dating resolves Klokken feldspar ^{40}K–^{40}Ar paradox", Earth and Planetary Science Letters **299**, 3-4, 426–433 (2010).

Hauri, E., J. Wang, J. E. Dixon, P. L. King, C. Mandeville and S. Newman, "SIMS analysis of volatiles in silicate glasses: 1. Calibration, matrix effects and comparisons with FTIR", Chemical Geology **183**, 1-4, 99–114 (2002).

Heiken, G., F. Goff, J. N. Gardner, W. Baldridge, J. Hulen, D. L. Nielson and D. Vaniman, "The Valles/Toledo Caldera Complex, Jemez Volcanic Field, New Mexico", Annual Review of Earth and Planetary Sciences **18**, 27 (1990).

Hervig, R. L., "Beryllium Analyses by Secondary Ion Mass Spectrometry", Reviews in Mineralogy and Geochemistry **50**, 1, 319–332, URL https://doi.org/10.2138/rmg.2002.50.8 (2002).

Hoskin, P. W., "SIMS Determination of μg g^{-1}-Level Fluorine in Geological Samples and its Concentration in NIST SRM 610", Geostandards Newsletter **23**, 1, 69–76 (1999).

Jochum, K. P., U. Weis, B. Stoll, D. Kuzmin, Q. Yang, I. Raczek, D. E. Jacob, A. Stracke, K. Birbaum, D. A. Frick *et al.*, "Determination of reference values for NIST SRM 610–617 glasses following ISO guidelines", Geostandards and Geoanalytical Research **35**, 4, 397–429 (2011).

Jochum, K. P., M. Willbold, I. Raczek, B. Stoll and K. Herwig, "Chemical Characterisation of the USGS Reference Glasses GSA-1G, GSC-1G, GSD-1G, GSE-1G, BCR-2G, BHVO-2G and BIR-1G Using EPMA, ID-TIMS, ID-ICP-MS and LA-ICP-MS", Geostandards and Geoanalytical Research **29**, 3, 285–302 (2005).

Koga, K., E. Hauri, M. Hirschmann and D. Bell, "Hydrogen concentration analyses using SIMS and FTIR: comparison and calibration for nominally anhydrous minerals", Geochemistry, Geophysics, Geosystems **4**, 2 (2003).

Kumamoto, K. M., J. M. Warren and E. H. Hauri, "New SIMS reference materials for measuring water in upper mantle minerals", American Mineralogist **102**, 3, 537–547 (2017).

Lodders, K., "Solar system abundances and condensation temperatures of the elements", The Astrophysical Journal **591**, 2, 1220 (2003).

Lucas, S. G. and A. B. Heckert, "Stratigraphy and correlation of Triassic strata around the Nacimiento and Jemez uplifts, northern New Mexico", Guidebook—New Mexico Geological Society **47**, 199–204 (1996).

Marks, M. A., M. A. Kendrick, G. N. Eby, T. Zack and T. Wenzel, "The F, Cl, Br and I Contents of Reference Glasses BHVO-2G, BIR-1G, BCR-2G, GSD-1G, GSE-1G, NIST SRM 610 and NIST SRM 612", Geostandards and Geoanalytical Research **41**, 1, 107–122 (2017).

Ottolini, L., "Accurate SIMS analysis of Ca in olivine based on high-energy doubly charged secondary ions", Journal of Analytical Atomic Spectrometry **17**, 3, 280–283 (2002).

Ottolini, L., P. Bottazzi and R. Vannucci, "Quantification of lithium, beryllium, and boron in silicates by secondary-ion mass spectrometry using conventional energy filtering", Analytical Chemistry **65**, 15, 1960–1968 (1993).

Padilla-Garza, R., "Geology of the Escondida porphyry copper deposit, Antofagasta region, northern Chile", Econ. Geol. **96**, 307–324 (2001).

Riciputi, L. R., W. Christie, D. R. Cole and T. M. Rosseel, "Analysis for rare earth elements in silicates by ion microprobe using doubly-charged ions", Analytical Chemistry **65**, 9, 1186–1191 (1993).

Riciputi, L. R., B. A. Paterson and R. L. Ripperdan, "Measurement of light stable isotope ratios by SIMS: Matrix effects for oxygen, carbon, and sulfur isotopes in minerals", International Journal of Mass Spectrometry **178**, 1-2, 81–112 (1998).

Rudnick, R. and S. Gao, "Composition of the continental crust", in "The Crust", edited by R. Rudnick, chap. 3, pp. 1–64 (Elsevier Science, 2003).

Schauer, S. N. and P. Williams, "Doubly charged sputtered ions of fourth-row elements", Physical Review B **46**, 23, 15452 (1992).

Shimizu, N. and S. Hart, "Applications of the ion microprobe to geochemistry and cosmochemistry", Annual Review of Earth and Planetary Sciences **10**, 1, 483–526 (1982).

Tenner, T. J., M. M. Hirschmann, A. C. Withers and R. L. Hervig, "Hydrogen partitioning between nominally anhydrous upper mantle minerals and melt between 3 and 5 GPa and applications to hydrous peridotite partial melting", Chemical Geology **262**, 1-2, 42–56 (2009).

Wang, Z. and H. Becker, "Abundances of sulfur, selenium, tellurium, rhenium and platinum-group elements in eighteen reference materials by isotope dilution sector-field ICP-MS and negative TIMS", Geostandards and Geoanalytical Research **38**, 2, 189–209 (2014).

Wedepohl, K. H., "The composition of the continental crust", Geochimica et cosmochimica Acta **59**, 7, 1217–1232 (1995).

Williams, P., "Secondary ion mass spectrometry", Annual Review of Materials Science **15**, 1, 517–548 (1985).

Wu, J., S. J. Cronin, M. C. Rowe, J. A. Wolff, S. J. Barker, B. Fu and S. Boroughs, "Crustal evolution leading to successive rhyolitic supereruptions in the Jemez Mountains volcanic field, New Mexico, USA", Lithos **396**, 106201 (2021).

Zinner, E. and G. Crozaz, "A method for the quantitative measurement of rare earth elements in the ion microprobe", International Journal of Mass Spectrometry and Ion Processes **69**, 1, 17–38 (1986).